

OBSERVATION OF THE FAR-ULTRAVIOLET CONTINUUM BACKGROUND WITH SPEAR/FIMS

KWANG-IL SEON^{1,2}, JERRY EDELSTEIN³, ERIC KORPELA³, ADOLF WITT⁴, KYOUNG-WOOK MIN⁵, WONYONG HAN^{1,2},
 JONGHO SHINN¹, IL-JOONG KIM¹, JAE-WOO PARK⁶

Draft version August 10, 2011

Abstract

We present the general properties of the far-ultraviolet (FUV; 1370–1710 Å) continuum background over most of the sky, obtained with the *Spectroscopy of Plasma Evolution from Astrophysical Radiation* instrument (SPEAR, also known as FIMS), flown aboard the STSAT-1 satellite mission. We find that the diffuse FUV continuum intensity is well correlated with N_{HI} , 100 μm, and H α intensities but anti-correlated with soft X-ray intensity. The correlation of the diffuse background with the direct stellar flux is weaker than the correlation with other parameters. The continuum spectra are relatively flat. However, a weak softening of the FUV spectra toward some sight lines, mostly at high Galactic latitudes, is found not only in direct-stellar but also in diffuse background spectra. The diffuse background is relatively softer than the direct stellar spectrum. We also find that the diffuse FUV background averaged over the sky has a bit softer spectrum compared to direct stellar radiation. A map of the ratio of 1370–1520 Å to 1560–1710 Å band intensity shows that the sky is divided into roughly two parts. However, this map shows a lot of patchy structures on small scales. The spatial variation of the hardness ratio seems to be largely determined by the longitudinal distribution of OB-type stars in the Galactic plane. A correlation of the hardness ratio with the FUV intensity at high intensities is found but an anti-correlation at low intensities. We also find evidence that the FUV intensity distribution is log-normal in nature.

Subject headings: diffuse radiation — dust, extinction — ISM: structure — radiative transfer — scattering — ultraviolet: ISM

1. INTRODUCTION

Measurement of the interstellar radiation field (ISRF), comprised of the direct-stellar and diffuse background radiation fields, is of considerable interest because the ISRF, in particular at the far-ultraviolet (FUV) waveband, controls the physics and chemistry of the interstellar medium (ISM). The FUV ISRF is often expressed by a simple approximation referred to as the Habing radiation field (Habing 1968) and was measured for the first time by Henry et al. (1977) with two Geiger counters on board an Aerobee rocket. Draine (1978) obtained another simple analytic expression that appeared to be in good agreement with all the previous results at that time, and it has been referred to as the Draine’s “standard” UV background. Gondhalekar et al. (1980) computed a theoretical model and tabulated the average UV ISRF scaled to fit the radiation field observed by the S2/68 telescope aboard the TD-1 satellite. Mathis et al. (1983) redetermined the ISRF by fitting the spectrum derived by Gondhalekar et al. (1980) to power-law and scaling up by 15% to bring it into better agreement with the measurement of Henry et al. (1980) and extended the

calculation to cover wavelengths from 0.09 μm to 1000 μm.

The majority of the diffuse FUV background radiation or the diffuse galactic light is generally believed to be of Galactic origin, starlight scattered off by interstellar dust. Observations of the diffuse background then give us information on the scattering properties of the dust grains. However, early attempts to measure the diffuse FUV background were motivated by the hope that a large fraction of the radiation in this waveband would be extragalactic (see reviews by Paresce & Jakobsen 1980, Bowyer 1991, and Henry 1991). There had been serious disagreements among observers regarding the spatial and spectral variabilities of the FUV background radiation. Discrepancies among early measurements of the diffuse FUV radiation have led to different interpretations as to its dominant contributor, either extragalactic light or galactic light scattered off dust grains. A correlation between the FUV background and Galactic neutral hydrogen column density (N_{HI}) was presented for the first time by Paresce et al. (1980), thereby implying that most of the FUV background is Galactic in origin, consistent with scattering of the integrated FUV radiation field by interstellar dust. Substantial evidence supporting the conclusion has been reported later (Maucherat-Joubert et al. 1980; Joubert et al. 1983; Jakobsen et al. 1984; Onaka & Kodaira 1991).

Some studies, however, have suggested that the correlation with Galactic latitude is more significant than that with Galactic H I column density (Weller 1983; Fix et al. 1989), or that the FUV background intensity shows only a weak correlation with Galactic observables (Murthy et al. 1989, 1990). However, Pérault et al.

¹ Korea Astronomy and Space Science Institute, Daejeon, Republic of Korea, 305-348; email: kiseon@kasi.re.kr

² University of Science and Technology, Daejeon, Republic of Korea, 305-350

³ Space Sciences Laboratory, University of California, Berkeley, CA, USA 94720

⁴ Ritter Astrophysical Research Center, University of Toledo, Toledo, OH, USA 43606

⁵ Korea Advanced Institute of Science and Technology, Daejeon, Republic of Korea 305-701

⁶ Korea Intellectual Property Office, Daejeon, Republic of Korea 302-701

(1991) confirmed the correlation with Galactic H I column density after subtraction of the inverse $\sin|b|$ dependence from the data obtained with the D2B-Aura satellite. Hurwitz et al. (1991) found that their data taken with the Berkeley UVX spectrometer was three times better in dependence with Galactic H I column density than with Galactic latitude. Jakobsen et al. (1987), Péault et al. (1991), and Sasseen & Deharveng (1996) showed also that a correlation exists between the diffuse infrared background intensity at $100\text{ }\mu\text{m}$ as measured by the Infrared Astronomical Satellite (IRAS) and the diffuse background intensity in the FUV wavelengths. Sasseen et al. (1995) demonstrated a similarity between the spatial power spectra of the IRAS $100\text{ }\mu\text{m}$ cirrus images and the diffuse FUV background images obtained with the Far Ultraviolet Space Telescope (FAUST). In the scale of a single cloud, Haikala et al. (1995) discovered a Galactic cirrus cloud, G251.2+73.3, near the north Galactic pole in FUV waveband and obtained a good correlation between the FUV intensity and IRAS $100\text{ }\mu\text{m}$ surface brightness. The existence of these properties thus provides strong observational support for the dust-scattered origin of most, if not all, of the FUV background.

Different contributors to the diffuse FUV background have been suggested as well. Duley & Williams (1980) proposed fluorescent H_2 emission as a significant contributor to the observed FUV background in addition to scattering by interstellar dust grains. Jakobsen (1982) showed that the reported correlations could be explained by a combination of starlight scattered by interstellar dust and the H_2 fluorescence. Later, the H_2 fluorescence emission lines from the diffuse ISM were observed with the Berkeley UVX Shuttle Spectrometer (Martin et al. 1990) and then by SPEAR (Lee et al. 2006, 2008; Ryu et al. 2006). Those measurements make it clear that the molecular hydrogen emissions are not the dominant contributor of the diffuse FUV background. Jakobsen & Paresce (1981) suggested that emission lines from a hot ($\gtrsim 10^5\text{ K}$) Galactic coronal gas would contribute to the diffuse FUV background, although this source would not be of sufficient intensity to influence the measurements of diffuse FUV continuum background. Deharveng et al. (1982) estimated the possible contribution of a warm ($\sim 10^4\text{ K}$) ionized medium (WIM) to the FUV background and attributed a FUV continuum intensity of $\sim 5 - 70\text{ photons cm}^{-2}\text{ s}^{-1}\text{ sr}^{-1}\text{ \AA}^{-1}$ (continuum unit, hereafter CU) to the two-photon continuum emission from the WIM (see also Hurwitz et al. 1991). Reynolds (1992) showed that the two-photon emission from the WIM accounts for approximately 20% of the diffuse FUV intensity near 1600 \AA .

Disagreements on the spectral shape of the diffuse FUV continuum background are also noticeable. Henry et al. (1978) measured the diffuse FUV background at the north and south Galactic pole regions, using a spectrometer flown on *Apollo 17*, and reported a spectrum that is flat between 1300 and 1525 \AA and declining in intensity toward 1625 \AA . The observations by Hua et al. (1979) and Zvereva et al. (1982) supported the decrease of intensity with increasing wavelength at high latitudes, using a spectrometer on board the Soviet spacecraft “Prognoz-6”. They also reported the flat spectrum in

the intermediate latitudes and a rapid increase of the intensity with wavelength near and inside the Milky Way. However, Anderson et al. (1979) reported some evidence for a sharp rise in intensity longward of 1680 \AA with instruments flown on an *Aries* sounding rocket. The data observed by Henry et al. (1980) also showed a rise longward of about 1500 \AA . Murthy et al. (1989) found a spectrally flat background over the wavelength band from 1200 to 1700 \AA with the Johns Hopkins UVX experiment on board the Space Shuttle. The spectrum obtained at a high Galactic latitude with the Berkeley UVX FUV spectrometer is relatively flat between 1400 and 1850 \AA (Martin & Bowyer 1990).

Such discrepancies would be better understood with spectrophotometric observations over large area of the sky. However, only a few studies have mapped a substantial fraction of sky in the FUV waveband. Gondhalekar et al. (1980) presented the spatial distribution of the FUV stellar radiation at four passbands centered at 1565 \AA , 1965 \AA , 2365 \AA , and 2740 \AA from observations made with the S2/68 sky-survey telescope. The first coarse map of the diffuse FUV radiation was presented by Lequeux (1990) and later updated by Péault et al. (1991) using the data obtained with the ELZ spectrophotometer on board the D2B-Aura satellite (see also, Maucherat-Joubert et al. 1978, 1980; Joubert et al. 1983). The most recent FUV band map is from the Narrowband Ultraviolet Imaging Experiment for Wide-Field Surveys (NUVIEWS; Schiminovich et al. 2001), which mapped one-quarter of the sky in FUV radiation ($\lambda = 1740\text{ \AA}$, $\Delta\lambda = 100\text{ \AA}$ FWHM) with $\sim 5' - 10'$ imaging resolution, including features such as the Upper Scorpions region.

Spectroscopy of Plasma Evolution from Astrophysical Radiation instruments (SPEAR, also known as Far Ultraviolet Imaging Spectrograph or FIMS) provided the first large-area spectral sky survey of diffuse FUV radiation (Edelstein et al. 2006a,b). The mission observed $\sim 80\%$ of the sky and conducted deep pointed observations toward selected targets, such as supernova remnants (Seon et al. 2006; Nishikida et al. 2006; Shinn et al. 2006, 2007; Kim et al. 2007, 2010a,b), superbubbles (Kregeow et al. 2006; Park et al. 2007; Ryu et al. 2008), photoionized H II regions (Park et al. 2010), and H_2 molecular clouds (Lee et al. 2006, 2008; Ryu et al. 2006; Park et al. 2009). The emission lines from multiply-ionized carbon, oxygen, silicon, and aluminum toward the north ecliptic and Galactic pole regions observed with SPEAR/FIMS were presented in detail by Korpela et al. (2006) and Welsh et al. (2007).

In this paper, we describe some general results on the diffuse FUV ($1370 - 1710\text{ \AA}$) continuum background observed with SPEAR/FIMS. Emission line sky-maps obtained with SPEAR/FIMS is described in Kregeow (2007) and Edelstein et al. (2011, in preparation). This paper is organized as follows. In §2 we describe the observation and data reduction. The FUV intensity maps, comparison of the diffuse FUV background with a model of the stellar radiation field are shown in §3. Spectral shapes of the diffuse FUV background is described in §4. We compare the diffuse FUV continuum map with maps of NHI , $\text{H}\alpha$, $100\text{ }\mu\text{m}$, and soft X-ray ($1/4\text{ keV}$) in §5. A discussion is presented in §6. Finally, we conclude with

a summary of results in §7.

2. OBSERVATION AND DATA REDUCTION

2.1. *Observation*

SPEAR/FIMS⁷ is a dual-channel FUV imaging spectrograph (“Short” wavelength channel [S-band] 900–1150 Å, “Long” wavelength channel [L-band] 1350–1750 Å; $\lambda/\Delta\lambda \sim 550$) with a large field of view (S-band, $4^\circ \times 4'.6$; L-band, $7^\circ.4 \times 4'.3$), designed to observe diffuse FUV emission lines. SPEAR is the primary payload on the first Korean science and technology satellite, *STSAT-1*, and was launched into a ~ 700 km Sun-synchronous orbit on 2003 September 27. The SPEAR/FIMS mission, the instruments, their on-orbit performance, and the basic processing of the instrument data are described in detail by Edelstein et al. (2006a,b). The spectrographs consist of the gratings, order baffling, the detector, a shutter-slit unit, a mirror unit with field baffling, and a deployable dust cover. The shutter can be selected to admit 0%, 1%, 10%, or 100% of the available light for safe and photometric observations of bright sources. The instrument provides for the first time accurate determination of the FUV background spectral map covering a substantial fraction of sky. The first Galactic map of diffuse FUV (L-band) background measured by SPEAR/FIMS was presented in Edelstein et al. (2006a). Because S-band lacks the Ly α -rejection filter that L-band has, the major continuum source for S-band is the instrumental background (Edelstein et al. 2006b; Kregenow 2007). In addition, S-band has lower sensitivity than L-band, as well as a higher non-astrophysical background, including a strong Ly β (1026 Å) airglow line. Therefore, in the present study, we analyze only the L-band data. Given the wavelength dependence of the dust albedo and the fact that the composite stellar spectrum, which is dominated by OB-type stars, peaks near L-band, we expect that the astrophysical continuum in S-band is no higher than in L-band.

SPEAR/FIMS observed the sky during the all-sky survey observation mode by scanning the entire sky along the short axis of the slit, i.e., along the $\sim 5'$ field direction of the $\sim 8^\circ \times 5'$ FOV. In each orbit, the FOV scanned $\sim 180^\circ$, from an ecliptic pole to the opposite ecliptic pole, during the eclipse time (~ 25 min), and the pole-to-pole scanning drifts 360° along the ecliptic equator for one year because of the properties of a sun-synchronous orbit. The FUV sky maps for L-band were created by binning photon and exposure events using the *HEALPix* tessellation scheme (Górski et al. 2005) with $\sim 1^\circ$ pixels (corresponding to the resolution parameter $N_{\text{side}} = 64$), unless otherwise specified, and L-band wavelength bins of 1.0 Å. Only the data from 1370 to 1710 Å, excluding the intense O I airglow line at 1356 Å, were used for the present analysis. The data were selected for attitude-knowledge quality by using times when the derived attitude error is $\leq 30'$ and contain 4.1×10^7 and 2.0×10^7 photons before and after removal of locally bright stars, respectively. The diffuse background map⁸ was obtained by eliminating photon and exposure events in the locally intense pixels (i.e., stars) from the starting sky map with

⁷ <http://spear.ssl.berkeley.edu/>.

⁸ The maps presented in the present study can be downloaded from the following URL: <http://kiseon.kasi.re.kr/FIMS.html>.

$\sim 14'$ pixels ($N_{\text{side}} = 256$). Each orbital scan was made into an image and convolved with an edge detection kernel shaped like the stellar point spread function. Any region with counts 3σ above the local background was considered a star. All photon events within a $3'$ radius of the star centroid were flagged in the data. This strategy effectively removed most faint and all bright stars (Edelstein et al. 2011, in preparation). The remaining photon and exposure events were binned into a map with $\sim 1^\circ$ pixels ($N_{\text{side}} = 64$).

We repaired orbit number mismatches that were found after the publication of Edelstein et al. (2006a,b), and included about 100 more orbits other than those used in Edelstein et al. (2006a). Sky exposure was derived by generating time-marked exposure events and mapping the events to a sky position as detailed in Edelstein et al. (2006a). The corresponding sky exposure map for the L-band with $\sim 1^\circ$ pixels ($N_{\text{side}} = 64$), shown in Figure 1, covers $\sim 80\%$ of the sky and includes features such as deep exposures (> 10 ks) toward calibration and pointed study fields. About 15% of these observations were taken using the 10% shutter position. The exposures taken with the 10% shutter aperture were scaled by 0.1, as determined in §2.2, and added to the map taken with the 100% shutter position. In the figure, the gray color represents locations with zero exposure.

In L-band, there are several spectral features, such as atomic emission lines (Si IV $\lambda 1398$, Si II* $\lambda 1532$, C IV $\lambda\lambda 1548, 1551$, and Al II $\lambda 1671$), quasi-band structures of H₂ fluorescence lines, and two-photon continuum emission. Since the physical processes that give rise to the emission lines are different than dominant continuum scattering, the variation of the emission lines may be independent from the dust-scattering processes that provide the bulk of the signal. If this emission is included when estimating the “continuum” intensity, the ability to compare the true FUV continuum background and other ISM tracers is weakened, as is any discussion of the statistical properties of the FUV continuum. To obtain the true intensity of the FUV continuum, we may have to model all possible emission lines and continuum using spectral fits, as in Korpela et al. (2006). However, the signal-to-noise ratio of the data with $\sim 1^\circ$ pixels is typically only ~ 10 (as described in §2.3), which is too small to provide reliable fits. To obtain reliable fits, large pixel sizes of $\sim 2^\circ - 7.5^\circ$ ($N_{\text{side}} = 32 - 8$) were required, especially at high Galactic latitudes, depending on locations in the sky (see also Edelstein et al. 2011, in preparation). In this paper, instead of using spectral fits and variable pixel sizes, we excluded the wavelength regions of the strongest emission lines (Si II*, C IV, and Al II, as shown in Figures 11 and 12) and averaged the data in the wavelength regions of 1310–1520 Å, 1560–1660 Å, and 1680–1710 Å. Unless otherwise specified, the FUV intensities in this paper were obtained in this way.

We report how the emission lines contribute to the total intensity of L-band. Edelstein et al. (2011, in preparation) showed that, on average, all atomic emission lines and H₂ fluorescence lines contribute about 5.1% and 2.9% (respectively) to the intensity of SPEAR/FIMS L-band. Our independent modeling using spectral fits indicated that the maximum contribution of emission lines is about 10%. Notably, the present results are not signif-

icantly different from results estimated using the whole L-band, which implies that the emission lines do not play a significant role in analyzing the general properties of the FUV continuum background. We therefore use the terms “diffuse FUV background” and “FUV continuum background” interchangeably. The contribution of two-photon emission to the diffuse FUV continuum background is discussed in §6.3.

2.2. Instrumental Background

The SPEAR/FIMS data are affected by instrumental (or detector) background due to cosmic rays, radioactive decay within the detector, and thermal charged particles entering the instrument. These background sources are relatively constant in time and uniform across the face of the detectors, implying that the instrumental background is spectrally flat intrinsically (Korpela et al. 2006; Krengeow 2007).

Since the instrumental background is independent of the size of the shutter aperture while the astrophysical signal is not, the background can be determined by comparing the data observed with both 100% and 10% shutter apertures toward the same sky. We thus determine the instrumental background rate assuming that the intensities measured with 100% and 10% shutter apertures are $I_{100\%} = I_{\text{sky}} + I_{\text{det}}$ and $I_{10\%} = aI_{\text{sky}} + I_{\text{det}} = aI_{100\%} + (1-a)I_{\text{det}}$, respectively. Here, a , I_{sky} , and I_{det} denote the scale factor between two shutter apertures, the sky intensity measured with 100% shutter aperture, and the detector background, respectively.

We first estimate the detector background intensity averaged over the whole L-band instead of applying the method to every spectral bin, and then calculate the instrumental background spectrum in terms of CU. We note that each pixel of a *HEALpix* map is hierarchically subdivided into many smaller pixels as the resolution parameter N_{side} increases. Some of the subdivided pixels from a non-zero-exposure pixel at $N_{\text{side}} = 64$ can have zero exposures, especially when the pixel is located at the boundary of each orbital scan. Hence, when comparing the 100% and 10% maps at $N_{\text{side}} = 64$, two coinciding pixels may not have the same sky coverage at higher resolutions. This discrepancy can produce a large variation when comparing 100% and 10% maps with $N_{\text{side}} = 64$. Thus, we only used pixels ($N_{\text{side}} = 64$) with 100% sky coverage at the level of $N_{\text{side}} = 256$, i.e., those pixels whose subdivided pixels at the level of $N_{\text{side}} = 256$ all have non-zero exposures. As shown in Figure 2, over the whole L-band, the averaged intensity of instrumental background that best fits the measurements is $\sim 190 \pm 10$ CU. Similar results that are consistent within $\sim 10\%$ were obtained using the higher or lower resolution parameters. In the fit, we fully adopted errors in both axes and found the best-fit linear straight line between the two intensities (Press et al. 1992). Because the noise-property of the SPEAR/FIMS data is dominated by photon-noise, we used only photon-noise in the present study. The estimated instrumental background was also justified by an arbitrary increase or decrease of the background intensity and through visual inspection of the combined map. Increasing or decreasing I_{det} by more than ~ 50 CU caused the observed sky regions with the 10% aperture to appear unrealistically bright or faint in the combined map. The scale factor between the two shutter apertures is

$\sim 0.10 \pm 0.01$ as originally designed.

Denoting the instrumental background rate by R_{det} counts $\text{s}^{-1} \text{\AA}^{-1}$ in the detector space, the instrumental background spectrum $I_{\text{det}}(\lambda_i)$ in units of CU in an i^{th} spectral bin is given by

$$I_{\text{det}}(\lambda_i) = \frac{R_{\text{det}} \Delta T \Delta \lambda}{A(\lambda_i) \Delta \Omega \Delta T \Delta \lambda} = \frac{R_{\text{det}}}{A(\lambda_i) \Delta \Omega}, \quad (1)$$

where $A(\lambda_i)$, $\Delta \Omega$, $\Delta \lambda$, and ΔT denote the effective area at the wavelength λ_i , solid angle, wavelength binsize, and exposure time, respectively. Applying the maximum likelihood method to Poisson data, the mean instrumental background intensity over the L-band is given by

$$I_{\text{det}} = \frac{\sum_i R_{\text{det}} \Delta T \Delta \lambda}{\sum_i A(\lambda_i) \Delta \Omega \Delta T \Delta \lambda} = \frac{R_{\text{det}} N_{\text{bin}}}{\sum_i A(\lambda_i) \Delta \Omega}, \quad (2)$$

where N_{bin} is the number of wavelength bins. We should note here that $I_{\text{det}} \neq \sum_i I_{\text{det}}(\lambda_i)/N_{\text{bin}}$. Thus the instrumental background spectrum is obtained by

$$I_{\text{det}}(\lambda_i) = I_{\text{det}} \frac{\sum_j A(\lambda_j)}{A(\lambda_i) N_{\text{bin}}}, \quad (3)$$

and is shown in Figure 3. In the figure, 1σ error limits are also shown in dotted lines. The spectrum of the instrumental background is inversely proportional to the effective area.

Using the solid angle of L-band $\Delta \Omega$ of $\sim 1.6 \times 10^{-4} \text{ sr}$ and average effective area $\sum_j A(\lambda_j)/N_{\text{bin}}$ of $\sim 0.19 \text{ cm}^{-2}$, we obtain the detector background rate $R_{\text{det}} = I_{\text{det}} \sum_j A(\lambda_j) \Delta \Omega / N_{\text{bin}} \sim 0.006 \text{ counts s}^{-1} \text{\AA}^{-1}$. The instrumental background was independently estimated to be $0.02\text{--}0.04 \text{ counts s}^{-1} \text{\AA}^{-1}$ by summing many shutter-closed dark exposures of 42 ks from 250 orbits (Edelstein et al. 2006b). Lee et al. (2006) adopted the same method and found a bit weaker detector dark background of about $0.01 \text{ counts s}^{-1} \text{\AA}^{-1}$. We note that the instrumental background rate estimated in the present study is even smaller than the value obtained by Lee et al. (2006). The discrepancy is attributable to the light leakage in shutter-closed dark exposures.

2.3. Basic Statistics

The histogram of the sky exposure is shown in Figure 4(a) on a logarithmic scale. The dotted line in the figure shows the exposure distribution for the data observed with the 10% shutter aperture only. Figure 4(b) shows the intensity distributions of the observed total FUV intensity ($I_{\text{FUV}}^{\text{total}}$) including both diffuse ($I_{\text{FUV}}^{\text{diffuse}}$) and direct stellar ($I_{\text{FUV}}^{\text{stellar}}$) intensities, and the diffuse FUV background only. The FUV background map has median and mean intensities of ~ 1250 and of ~ 3170 CU, respectively. The reason for the difference between the median and mean values are obvious from the asymmetry of the intensity histogram. The difference in the median value from Edelstein et al. (2006a) is mainly due to subtraction of the instrumental background and inclusion of more orbits. The total FUV intensity map has median and mean intensities of ~ 1610 and ~ 7080 CU, respectively. The distribution of signal-to-noise ratio is also shown in Figure 4(c). For $\sim 1^{\circ}$ ($N_{\text{side}} = 64$) pixels, about 84% and

87% of pixels have significance of 3σ or higher from the diffuse FUV sky and the total sky, respectively. Mean and median signal-to-noise ratios of $I_{\text{FUV}}^{\text{diffuse}}$ are ~ 13 and ~ 10 , respectively, and the ratios of $I_{\text{FUV}}^{\text{total}}$ are ~ 17 and ~ 10 , respectively. The statistical properties of the FUV intensities estimated over the whole L-band including the strong emission line regions are not significantly different.

3. FUV INTENSITY

3.1. Morphology

The maps of the total intensity ($I_{\text{FUV}}^{\text{total}}$) and the diffuse background intensity ($I_{\text{FUV}}^{\text{diffuse}}$) observed with SPEAR/FIMS are shown in Figure 5 and 6 together with the signal-to-noise ratio maps. As observed by Henry et al. (1977) and Gondhalekar et al. (1980), the sky is strongly anisotropic in FUV. Not only is there a strong variation with Galactic latitude, but also with longitude. For example, much more FUV radiation is observed between longitude 180° and 360° than between 0° and 180° in the Galactic plane. Gould's belt, inclined at $\sim 18^\circ$ to the Galactic plane with the direction of tilt toward Orion, shows up well in Figure 5 (Stothers & Frogel 1974; Elias et al. 2006 and references therein).

Obviously, the diffuse FUV background seems to follow direct starlight in general. However, it will be shown in §3.3 and §5 that $I_{\text{FUV}}^{\text{diffuse}}$ correlates better with dust, traced by $100\ \mu\text{m}$ emission, and H I column density rather than with the direct stellar intensity. The largest diffuse intensity is toward the Galactic plane and other regions where bright early-type stars coexist with suitable columns of interstellar dust, such as the obvious feature of the Sco-Cen association and the Vela region. We note that the sky is brightest at the Vela region in both the total and diffuse background intensities.

We confirm the existence of a significant depression in both the diffuse and total FUV maps at high latitudes above less intense segments of the Galactic plane from $l = 20^\circ$ to $l = 60^\circ$, as noted in Schiminovich et al. (2001) and Gondhalekar et al. (1980). Gondhalekar et al. (1980) showed that this direction corresponds to one of the most heavily reddened directions in the sky by comparing the FUV map with the reddening data of Nandy et al. (1978). We also confirmed the strong reddening toward this direction with the more recent results given by Arenou et al. (1992), Chen et al. (1998), and Joshi (2005). The dark region in $15^\circ < l < 40^\circ$ and $-6^\circ < b < +20^\circ$ is in fact a molecular cloud referred to as Aquila Rift, which emits strong CO line emission and has a maximum extinction of $Av \sim 3$ (Dame & Thaddeus 1985; Straizys et al. 2003).

As can be seen in the orthographic projections of Figure 6(b), the map reveals lots of detectable structures everywhere in the sky. A full examination of the rich detail in the diffuse FUV map observed by SPEAR/FIMS is beyond the scope of this paper. However, it would be worthwhile to note that a large structure centered at $(l, b) \sim (316^\circ, 51^\circ)$ is a feature produced by dust-scattered off starlight from a B1III/IV + B2V spectroscopic binary α Vir with a distance of 87 pc (Park et al. 2010). An H II region surrounding the star has been detected by Reynolds (1985).

3.2. Dependencies on Galactic Coordinates

Figures 7 and 8 examine the distribution of $I_{\text{FUV}}^{\text{diffuse}}$ as a function of Galactic coordinates. The top panel of each figure plots a two-dimensional histogram in the space of intensity versus coordinates, while the bottom panel shows the median and the standard deviation of intensities from the median value within each of coordinate bins. The sharp cutoff at low intensities in Figure 4(b) and the shape of the latitude profile of the diffuse FUV emission in Figure 8 resemble the corresponding features shown in the diffuse H α emission (Figures 10 and 11, respectively, in Haffner et al. 2003). These similarities between the diffuse FUV and H α emissions may be explained to some extent by a simple plane-parallel model. In the idealized model, the cosecant effect is removed by plotting $I_{\text{FUV}}^{\text{diffuse}} \sin |b|$ versus $\sin |b|$. This is examined in Figure 9. The top panel again plots a two-dimensional histogram and the bottom panel shows the median and standard deviation, with the trend for the northern Galactic hemisphere split from that of the southern hemisphere. It should be noted, however, that the plane-parallel model turns out to be only approximate in describing the diffuse FUV background, as is also the case for the H I gas and the WIM (Dickey & Lockman 1990; Haffner et al. 2003). The horizontal line in Figure 9 delineates the overall median value of $I_{\text{FUV}}^{\text{diffuse}} \sin |b| = 525.4$ CU. The decrease in $I_{\text{FUV}}^{\text{diffuse}} \sin |b|$ at $\sin |b| < 0.05$ (i.e., $|b| < 3^\circ$) is attributed to a strong dust extinction in the Galactic disk.

The diffuse FUV intensity decreases from $\sin |b| = 0.2$ through 1.0 in both Galactic hemispheres. Similar effects have been observed in the H α and H I distributions, and the departure from the $\csc |b|$ law was attributed at least in some extent to the presence of the Local Bubble (Cox & Reynolds 1987), a localized region of very low-density gas around the Sun, as pointed out by Dickey & Lockman (1990) for H I. Since the Local Bubble is believed to be elongated perpendicular to the Galactic plane (Lallement et al. 2003), a larger fraction of column density of the ISM is carved out at high latitudes, yielding the apparent departure from the $\csc |b|$ law. However, the main reason for the departure in the diffuse FUV background is due to the larger contribution of dust-scattered FUV radiation at low latitude, as shown for the H α radiation by Wood & Reynolds (1999).

3.3. Comparison with Stellar Radiation Fields

Henry (1977) showed that simple addition of the predicted UV light from all of the stars listed in common star catalogs provides an estimate of the expected ISRF in the UV band which is in good agreement with the more complex models (see also, Henry et al. 1977). Thus, we made a model of direct starlight using the *Hipparcos* catalog (Perryman et al. 1997; van Leeuwen 2007) for stellar location, distance, spectral type, and brightness. The *Hipparcos* catalog has a limiting magnitude of $V \sim 12.4$ and was chosen for the calculation of three-dimensional locations of stars. The model is basically the same as in Henry & Murthy (1993), Henry (2002), and Sujatha et al. (2004).

Based on the spectral type of each star, we derived a temperature and effective gravity using the tables from Straizys & Kurliene (1981) and calculated a spectral energy distribution for each star with a new grid of Ku-

rucz models (Castelli & Kurucz 2003), rather than using the original grid of Kurucz models. The intrinsic FUV luminosity of each star was obtained by scaling the model flux with the factor derived from the formula, as in Sujatha et al. (2004):

$$\frac{4\pi R^2}{4\pi d^2} F_V e^{-\tau_V} = (f_V)_0 10^{-V/2.5}, \quad (4)$$

where R^2 is the scaling factor corresponding to the stellar radius, d the distance from the Sun, $(f_V)_0 = 3.631 \times 10^{-9}$ ergs cm $^{-2}$ sec $^{-1}$ Å $^{-1}$ the absolute visual magnitude corresponding to zero magnitude (Bessell et al. 1998), F_V the model flux (ergs cm $^{-2}$ sec $^{-1}$ Å $^{-1}$) at V band filter, V the observed Johnson magnitude, and τ_V the optical depth at V band filter which can be estimated from $\tau_V = A_V / 1.0863$. Here, the absolute visual magnitude is calculated from the standard relation $A_V = R_V E(B-V)$ and $R_V = 3.1$, and the color excess $E(B-V)$ obtained from the observed $B-V$ and the theoretical $B-V$ as derived from the Kurucz model spectrum. In many cases multiple or complex spectral types were associated with a single star; in such cases, we used the first listed spectral type. We then integrated the stellar flux attenuated by the dust distribution along given lines of sight. The resulting stellar fluxes in every pixel are summed up to yield the “stellar equivalent diffuse intensity (SEDI)” as defined by Hurwitz et al. (1991):

$$I_{\text{SEDI}}^{\text{Hipparcos}} = \sum_{i=1}^{\text{all stars}} \frac{L_i}{4\pi d_i^2} \frac{1}{\Omega_{\text{Healpix}}} e^{-\tau_i}, \quad (5)$$

where L_i is the luminosity of each star at the 1370–1710 Å band (excluding the strongest emission line regions) in photons s $^{-1}$ Å $^{-1}$, d_i is the distance to the star in centimeters, τ_i is the optical depth to each star at the waveband, and $\Omega_{\text{Healpix}} = 4\pi/N_{\text{pix}}$ is the solid angle (steradians) of a pixel. The optical depth at the FUV wavelength is calculated by $\tau_{\text{FUV}} = 2.86(\sigma_{\text{FUV}}/\sigma_V)E(B-V)$ where σ_{FUV} and σ_V are the dust extinction cross-sections at the FUV wavelength and the V band filter for the average Milky Way dust with $R_V = 3.1$ as from Weingartner & Draine (2001) and Draine (2003). We used the resolution parameter $N_{\text{side}} = 32$ corresponding to an angular resolution of $\sim 1.8^\circ$ and the number of pixels $N_{\text{pix}} = 12,288$ in order to increase the number of pixels including stars.

We also calculated the SEDI using the TD-1 stellar catalog (Thompson et al. 1978). The TD-1 satellite performed the first UV all-sky survey and measured the absolute UV fluxes of point sources down to the tenth visual magnitude for unreddened early B stars. The TD-1 catalog presents the stellar fluxes in four bands (each 310–330 Å wide, centered at 1565, 1965, 2365, and 2740 Å) for 31,215 stars. The SEDI of the TD-1 stars is defined by $I_{\text{SEDI}}^{\text{TD-1}} = \sum_i F_i / \Omega_{\text{Healpix}}$ using the stellar fluxes F_i at the 1565 Å band. Schiminovich et al. (2001) also used the TD-1 star catalog to model the diffuse FUV background, and they found that stars with 10 times higher flux than the TD-1 catalog cutoff contribute about 21 CU to the FUV background. Therefore, the TD-1 catalog is complete enough for the analysis of the diffuse FUV background.

First of all, the TD-1 SEDI is compared with the *Hip-*

parcos SEDI and the direct stellar intensity obtained from SPEAR/FIMS data in Figures 10(a) and (b), respectively. The *Hipparcos* SEDI predicts the TD-1 SEDI very well in the statistical sense. However, the *Hipparcos* SEDI is a bit higher than the TD-1 SEDI at intensities lower than ~ 100 CU, implying that the stars in the TD-1 catalog are not complete down to the intensity level that was estimated with the *Hipparcos* catalog, although the incompleteness is not so significant. Larger scatters in Figure 10(b) than those shown in Figure 10(a) are mainly due to the coarse algorithm used to identify stars in the SPEAR/FIMS data analysis. However, the correlation between the TD-1 SEDI and the SPEAR/FIMS $I_{\text{FUV}}^{\text{stellar}}$ is good enough to move into the following arguments.

We note in Figures 10(c) and (d) that $I_{\text{FUV}}^{\text{diffuse}}$ shows more or less a general correlation with the *Hipparcos* and TD-1 SEDIs. However, as noted by Hurwitz et al. (1991), as long as one avoids the brightest early-type stars in the sky by more than a few degrees, there should not be a strong correlation between line-of-sight starlight and line-of-sight dust illumination. In fact, we found that the correlation with the direct stellar intensity is rather weaker than that with the infrared 100 μm emission and N_{HI} , as discussed in §5. It is also obvious that the $I_{\text{FUV}}^{\text{total}}$ is brighter than both SEDIs, as in Figures 10(e) and (f), especially at relatively low intensities $I_{\text{FUV}}^{\text{total}} \lesssim 10,000$ CU. The deviation of $I_{\text{FUV}}^{\text{total}}$ from the *Hipparcos* and TD-1 SEDIs increases as the SEDIs decrease. This trend is a direct result of the intensity distribution of $I_{\text{FUV}}^{\text{diffuse}}$ as can be seen in Figures 10(c) and (d), in which $I_{\text{FUV}}^{\text{diffuse}}$ shows no strong correlation with the SEDIs. More specifically, within each “pixel” ($\sim 1.8^\circ$), there is an excess of diffuse FUV, which is above the estimate from the stellar fluxes that are directly detected and/or modeled within that pixel and does not correlate with the direct stellar flux in the pixel. For low-intensity pixels, the excess of diffuse FUV would mainly be due to dust-scattered light from stars that are not located along the line of sight of the pixels. The conclusion is discussed much more clearly in §4.2, which attempts to link a harder spectrum at low intensities to this excess. In fact, luminous UV stars produce extended dust-scattered halos that are far greater than the volume sample of the pixels here (e.g., Murthy & Henry 2011). We thus conclude that simply adding stellar flux underestimates ISRF, especially at the low intensity of $I_{\text{ISRF}} \lesssim 10,000$ CU, against the results of Henry (1977) and Henry et al. (1977). Three-dimensional radiative transfer models may help to assert what portion of the ISRF is the result of the dust-scattered FUV background.

It would be worthwhile to note that the contribution of unresolved faint stars to our diffuse FUV background map is negligible. The diffuse background or the total intensity would be correlated at low intensity pixels with the model SEDI if this was the case. However, it is obvious in Figure 10(c) and (d) that this is not the case. The difference of more than an order between I_{SEDI} and the mean value of $I_{\text{FUV}}^{\text{total}}$ at $I_{\text{SEDI}} \sim 50$ CU in Figures 10(e) and (f) is unlikely due to the contribution from unresolved stars. We thus conclude that residual starlight is not a significant contributor to the diffuse FUV background. The contribution from faint stars seen in Fig-

ure 10(a) is much smaller than the difference between I_{SEDI} and $I_{\text{FUV}}^{\text{total}}$ in Figures 10(e) and (f). Many studies (i.e., Hurwitz et al. 1991; Henry 2002) have estimated the contribution of unresolved faint stars with several methods in their analysis of the FUV background data, and they all have concluded that the contribution is not significant. Additional support for this conclusion will be provided in §4 from an argument based on hardness ratio. We also note that the large difference between the diffuse FUV intensity and the model SEDIs cannot be due to H₂ fluorescence lines and two-photon continuum emission, which may account for $\sim 2.9\%$ (Edelstein et al. 2011, in preparation) and $\sim 4 - 9\%$ (see §6.3) of the diffuse intensity, respectively.

Zodiacal light, sunlight scattered by interplanetary dust, is also negligible at these wavelengths since the solar G0 spectrum falls steeply at the FUV wavelengths (Tennyson et al. 1988), and we have confirmed that our data show no systematic trend with ecliptic latitude. Scattering of diffuse Ly α radiation (geocoronal/interplanetary) as determined from laboratory measurements is also negligible. The insignificance of unresolved faint stars, zodiacal light, and Ly α scattering is also justified from the agreement of the so-called “isotropic component” estimated in §5 with the previous measurements.

4. FUV SPECTRUM

4.1. Spectral Variations

The direct stellar and diffuse background intensities should show strong anisotropy not only in intensity but also in spectral shape. In Figures 11 and 12, the average spectra of the diffuse background, direct starlight, and total radiation in various Galactic longitude and latitude ranges, respectively, are shown. The direct stellar spectra were obtained by subtracting the diffuse background spectra from the total spectra in each coordinate range. We note that the FUV intensities are strongest in $240^\circ < l < 270^\circ$ and in $-10^\circ < b < 0^\circ$, where the Vela region is located, as was seen in Figure 6. The Vela region is the brightest not only in emission lines due to the Vela supernova remnant but also in the FUV continuum (cf. Nishikida et al. 2006).

The average background intensity is about the same as the direct stellar intensity in all coordinate ranges shown in the figures, and the total intensity is approximately two times higher than the direct stellar intensity. Ignoring the latitude range $b < -10^\circ$, where exposures and signal-to-noise ratios are small, the intensity ratio of the diffuse background to the direct starlight decreases with Galactic latitude, and then increases at the highest latitude range of $70^\circ < b < 90^\circ$. The trend is easily understandable, at least qualitatively, by adopting the results from a simplified spherical dust model with an embedded source. The scattered to absorbed stellar flux ratio in the model increases monotonically with optical depth and can easily be of the order of unity or higher for optical depth of $\tau = 1 - 2$ (Witt et al. 1982). The optical depth of $\tau \sim 1.26$ at 1550 Å is estimated at $N_{\text{HI}} = 1 \times 10^{21} \text{ cm}^{-2}$ using the standard gas-to-dust ratio (Bohlin et al. 1978) and the Milky Way dust extinction cross-section (Weingartner & Draine 2001; Draine 2003). Therefore, the approximate equality between the diffuse and direct

stellar intensities at the Galactic plane is obtained. The decrease of the diffuse to direct stellar intensity ratio with Galactic latitude is also explained since the optical depth decreases with latitude. However, at the highest Galactic latitude range $70^\circ < b < 90^\circ$, the “isotropic component” of ~ 300 CU discussed in §6 contributes significantly to the diffuse background in addition to the scattered radiation of Galactic starlight in the latitude range, and thus causes the ratio to increase.

A weak rise in the diffuse spectra longward of about 1550 Å is shown in most of the latitudes in Figure 12, although the FUV continuum spectra are flat in general. However, the dependence of the rise on the Galactic latitude is not clear. The rise is also noticeable at $120^\circ < l < 180^\circ$ in Figure 11, where most of observations were performed at high latitudes as seen in Figure 1. It should be noted as well that the softer the diffuse spectrum is, the softer the direct stellar spectrum also is. A much sharper rise longward of ~ 1550 Å than that found here was obtained by Henry et al. (1980), in which they concluded that the rise was due to very large numbers of faint stars contributing to the ISRF. Later, Henry (2002) reanalyzed the data and attributed the rise to an actual rise in the interstellar grain albedo. However, these features may not be due to a single cause. Firstly, a stronger extinction at a shorter wavelength leads to the reddening or softening not only of direct stellar, but also of diffuse spectra, unless the dust albedo decreases with wavelength as will be shown in §6 (Figure 25). Secondly, if there is no significant contribution from bright early-type stars near a given sight line, faint late-type stars should contribute, at least in part, to the spectra in addition to the dust-scattered light from distant early-type stars.

It should also, more importantly, be noted that the diffuse background spectrum is always softer than the direct stellar spectrum. The rise of the dust albedo with wavelength is in fact closely related to the relative softness of the scattered to the direct stellar spectra, as will be discussed in §6. We also note that both the direct stellar and diffuse spectra are harder, or bluer, in the Galactic longitude range $240^\circ < l < 270^\circ$, where the Vela region dominates the radiation field, than other longitude ranges, implying the existence of lots of hot stars and/or less extinction in the region. A relatively sharp rise longward of about 1690 Å at $|b| > 50^\circ$ is also found mostly in the diffuse background spectrum. However, the origin of this rise is not clear at this time.

We now compare the spatially-averaged total (direct stellar + diffuse) FUV spectrum observed with SPEAR/FIMS with the previous models and observations in Figure 13. It can be easily noted that all previous results are higher, up to a factor of more than 3 for the Draine’s model, than the SPEAR/FIMS data. In Figure 12, the observed total spectrum is stronger only at $-10^\circ < b < 0^\circ$ than the Draine’s “standard” radiation field, while the intensities in other latitude ranges are in general weaker. The relative weakness of the observed data compared to the model ISRFs indicates that the previous works are mostly biased toward bright regions in Galactic plane. In Figure 13, we also plotted the average spectra of the diffuse background and the direct starlight. The figure shows once again that the direct starlight and the diffuse background contributes

approximately the same amounts to the total spectrum on average, implying underestimation of the ISRF when only direct starlights are added.

The spectral shapes of the model ISRFs calculated by [Gondhalekar et al. \(1980\)](#) and the Habing field are more or less similar to the SPEAR/FIMS data, while the Draine’s “standard” and Mathis background radiation fields are a bit harder than that of SPEAR/FIMS. The observed spectrum of [Henry et al. \(1980\)](#) is softer than the SPEAR/FIMS data. We also note that the diffuse background spectrum averaged over all the sky is a bit softer than the stellar spectrum, and that discrete spectral features such as atomic emission lines are mainly shown in the diffuse spectrum only, as already shown in Figures 11 and 12. The relative softness or redness of the diffuse background compared to the direct stellar spectrum is once again attributed to rise of the dust-scattering albedo at a longer wavelength, as will be discussed in §6.

4.2. Hardness Ratio

In order to further investigate spectral variations of the diffuse background, we plotted a map of the hardness ratio defined as the ratio of average intensities at $\lambda\lambda 1370 - 1520$ Å and at $\lambda\lambda 1560 - 1710$ Å (excluding $\lambda\lambda 1660 - 1680$ Å to avoid the Al II emission line) in Figure 14. In the figure, we selected a color scheme to represent the region with relatively blue or hard spectra as blue colored. The spectral hardness map shows highly patched structures and no clear trend along with Galactic latitudes. Instead, we note that the sky can be largely divided into two blocks mainly along Galactic longitudes. In fact, we smoothed the hardness ratio map using a gaussian kernel with full width at half maximum of $\sim 3.5^\circ$ and saturated the color range to clarify the division of the sky based on the hardness ratio. A bit harder radiation is observed between longitude 180° and 360° , where stronger radiation is found in Figure 6, than between 0° and 180° . Interestingly, we found that the hardness ratio of the diffuse background follows in general the spatial distribution of OB-type stars in the Galactic plane. In Figure 15, we plotted maps for numbers of OB-type stars and of A-type stars using the TD-1 stellar catalog. We note from the figure that the Galactic plane can be divided into three regions: $240^\circ < l < 360^\circ$ where OB-type stars are predominantly found, $30^\circ < l < 90^\circ$ and $180^\circ < l < 240^\circ$ where A-type stars are dominant, and $90^\circ < l < 150^\circ$ where both OB- and A-types are rare. In the Galactic longitudes where OB-type stars are dominant, the hardness ratio is generally higher than the other regions.

We also plotted the ratio versus Galactic longitude and latitude in Figures 16 and 17, respectively. In Figure 16, the median value of the hardness ratio at each longitude bin is generally lower in $0^\circ < l < 180^\circ$ than in $180^\circ < l < 360^\circ$. On the other hand, Figure 17 shows no clear trend along Galactic latitude. In order to confirm the close relation between the hardness ratio and the number of OB-type stars, we calculated the average hardness ratio and the number of OB-type stars within each of the 3° longitude bins, and plotted the average hardness ratio versus the number of OB-type stars in Figure 18. The figure shows a clear correlation between the average hardness ratio and the number of OB-type

stars. We also note a dip at $120^\circ < l < 180^\circ$ in Figure 16. The dip does not seem to be an artifact caused by a relatively low exposure at low latitudes in this longitude range. In the light of the argument described in the previous paragraph, the softness in the longitude region would be a direct consequence of no bright stars in the range.

Figure 19 shows the hardness ratio versus the diffuse FUV intensity. Rises of the hardness ratio at high and low intensities are noted in the figure. To understand the trend, we calculated the hardness ratio versus the direct stellar intensity using the previous stellar model; the result is shown in Figure 20. In the calculation of the hardness ratio, we incorporated the wavelength dependence of dust extinction as well. We note that the model ratios predict the observed values nicely at high intensities ($I_{\text{FUV}}^{\text{diffuse}} > 2000$ CU), of which most of the radiation is from low Galactic latitudes. Therefore, we attribute the rise of the hardness ratio at high intensities ($I_{\text{FUV}}^{\text{diffuse}} > 2000$ CU) mostly to the spectral hardness of stars that are located at low Galactic latitudes.

However, the slight rise of the hardness ratio at low intensities ($I_{\text{FUV}}^{\text{diffuse}} < 2000$ CU) cannot be explained by stellar types at high Galactic latitudes. One possible explanation for this rise is the contribution of dust-scattered starlight from earlier stars rather distant than nearby stars that are located along the same line of sight for each pixel. This is supported by Figures 10(c) and (d), which show clear excesses of the diffuse background above the nearby direct stellar intensity. In fact, our preliminary results of the Monte Carlo simulation, which will be presented in detail elsewhere, show that B-type stars are significant sources of the diffuse FUV background even at the high Galactic latitudes where most stars are A-types. [Henry \(2002\)](#) also noted that B-type stars contribute the largest amount to the ISRF in his simplified model. We thus conclude that both the rise of the hardness ratio and the excess of the diffuse background over the direct stellar intensity at low intensities are largely due to the contribution of B-type starlight scattered off dust grains. However, at the lowest intensities of less than a few hundred CU, the “isotropic component” would contribute significantly. A detailed study on the relative significance between the two components may need extensive radiative transfer models that are beyond the scope of this paper.

5. COMPARISON WITH VARIOUS GALACTIC QUANTITIES

We now examine correlations of the observed FUV background with various galactic quantities, not only with the H I column density and 100 μm emission but also with the H α and soft X-ray (1/4 keV) emissions. Although extensive correlation studies between the diffuse FUV background, the H I column density, and 100 μm emission have been performed, no detailed correlation study with other waveband observations has been done. The all-sky map of H I column density are from the Leiden/Argentine/Bonn (LAB) Survey ([Kalberla et al. 2005](#)). The 100 μm and H α emission maps are from [Schlegel et al. \(1998\)](#) and [Finkbeiner \(2003\)](#), respectively. The soft X-ray (1/4 keV) map is from the *ROSAT* All-Sky Survey (RASS) map ([Snowden et al. 1997](#)). The H I data interpolated onto a HEALPix projection were

obtained from the Legacy Archive for Microwave Background Data Analysis (LAMBDA).

Correlations between the diffuse FUV intensity and other quantities are shown in Figure 21 in log-log scales. Two-dimensional histogram images and contours are shown in the figure instead of the usual pixel-by-pixel comparison to clarify their correlation. Correlation coefficients estimated in logarithmic scale are also shown in Figures 21. It is also worthwhile to note that the correlation coefficient between the diffuse FUV background and the direct stellar radiation is ~ 0.46 , much less than those for N_{HI} and $I_{100\mu\text{m}}$. In Figure 22, we examine the correlations in linear-linear scales, especially at high Galactic latitudes ($b > 25^\circ$). The general similarity in the latitude dependence of the data sets (the H I column density, 100 μm , H α , and FUV emissions) may dominate their correlations. To reduce the latitude dependence, we therefore calculated the average intensities multiplied by $\sin|b|$ within each of the $\Delta \sin|b| = 0.02$ latitude intervals. The correlations between the quantities multiplied by $\sin|b|$ are shown in Figure 23, in which only the data sets observed at high Galactic latitudes ($|b| \geq 30^\circ$) were examined, in order to minimize the dust extinction effect at low Galactic latitudes. The numbers outside and inside the parentheses in Figure 23 are correlation coefficients calculated in linear and logarithmic scales, respectively. Here, we note that Figure 23 shows strong correlations between emission tracers, implying that the correlations between the FUV background and other emission tracers are not simply due to the latitude dependence of the Galactic observables.

5.1. Correlation with N_{HI} and $100\mu\text{m}$ emission

Correlation plots of the diffuse FUV background with H I column density and 100 μm intensity are shown in Figures 21(a) and (b), respectively. There is large scatter in the correlation plots. We note that the diffuse FUV continuum intensity saturates at about $N_{\text{HI}} \sim 10^{21} \text{ cm}^{-2}$, which was found for the first time by Hurwitz et al. (1991). The same effect of saturation is also shown in comparison with the 100 μm intensity. This saturation at a high intensity can be attributed to strong dust absorption of the FUV radiation at low Galactic latitudes. Flattening at a low intensity, which has been often attributed to extragalactic background, is also seen in Figures 21(a) and (b).

As is obvious in the figures, the diffuse FUV intensity for a given N_{HI} or 100 μm brightness varies more than by a factor of 2–3, up to an order of magnitude, with directions in the sky. Witt et al. (1997) argued that most of the observed variation is a result of the spatially, severely anisotropic, ISRF. Since the diffuse FUV background depends not only on the interstellar dust but also on the in-situ stellar radiation field, the usual pixel-by-pixel comparison might be affected by the strong anisotropic stellar radiation field. We thus averaged the FUV data corresponding to a given H I column density or a given 100 μm brightness and compared the average FUV intensity with N_{HI} and 100 μm brightness. In this way, the effect of the spatially varying stellar radiation field may be averaged, and only the effect due to H I or dust column density can be investigated. The average FUV intensity versus N_{HI} and $I_{100\mu\text{m}}$ are shown in Figure 22, together with the best regression lines. In the figure, the data

used in the fit are denoted by filled circles, and the data not used in the fit by hollow circles. In the fit, we used only the data for $b > 25^\circ$. The best-fit regression lines are given by

$$I_{\text{FUV}}^{\text{diffuse}} = (1.49 \pm 0.07) \times \frac{N_{\text{HI}}}{10^{18} \text{ cm}^{-2}} + (271.2 \pm 26.7) \text{ CU}, \quad (6)$$

and

$$I_{\text{FUV}}^{\text{diffuse}} = (158.3 \pm 11.7) \times \frac{I_{100\mu\text{m}}}{\text{MJy/sr}} + (243.1 \pm 44.4) \text{ CU} \quad (7)$$

for H I column density and 100 μm emission, respectively.

Paresce et al. (1980) reported variations in the slopes and brightness axis intercepts corresponding to the various scans. As noted by Jakobsen et al. (1984), there is no unique, canonical relationship between background intensity and a hydrogen column density that is obeyed everywhere in the sky. Principally, this result is not surprising, since the detailed viewing geometry and the illuminating UV stellar radiation field are highly anisotropic, and several of the physical parameters, such as dust properties, are expected to vary from region to region in the ISM. However, it is obvious, as shown in Figure 21(a) and (b), that there is a general correlation in the global scale between the diffuse FUV background and both the neutral hydrogen column density N_{HI} and IR 100 μm emission. The linear correlation has been measured by many different investigators, and the results published before 1991 were summarized in Bowyer (1991) as $I_{\text{FUV}}^{\text{diffuse}} \simeq (0.3\text{--}2.5) \times (N_{\text{HI}}/10^{18} \text{ cm}^{-2}) + 300 \text{ CU}$, which is consistent with our result.

The flaring and large scatters shown in these linear-linear correlation plots are in general due to large variations of the diffuse FUV intensity as noted in the log-log correlation plots of Figure 21. Note that the larger scatters are found at the higher mean intensities, the property that will be discussed in more detail in §6. We also note a straight-line correlation for $I_{100\mu\text{m}} < 8 \text{ MJy/sr}$ in Figure 22(b). Witt et al. (2008) found that there was also a linear correlation between the optical surface brightness of high-latitude cirrus clouds and their 100 μm intensity at least up to $\sim 8 \text{ MJy/sr}$. This is the range in which these objects remain optically thin and single scattering by dust grains is dominant. The systematic deviation from a straight-line correlation for $I_{100\mu\text{m}} > 8 \text{ MJy/sr}$ in Figure 22(b) would be due to the fact that at the higher $I_{100\mu\text{m}}$ values we are entering lower galactic latitudes where the effects of the strongly forward-directed scattering phase function of dust produces strongly enhanced FUV intensities compared to those produced by the scattering at mostly larger scattering angles at higher latitudes, where the 100 μm intensities are generally low.

5.2. Correlation with the Diffuse H α Emission

In linear scale, the best regression line between $I_{\text{FUV}}^{\text{diffuse}}$ and $I_{\text{H}\alpha}$ is given by

$$I_{\text{FUV}}^{\text{diffuse}} = (456.0 \pm 23.5) \times \frac{I_{\text{H}\alpha}}{R} + (309.2 \pm 31.4) \text{ CU}, \quad (8)$$

where R denotes Rayleigh ($1 \text{ R} = 10^6/4\pi \text{ photons cm}^{-2} \text{ s}^{-1} \text{ sr}^{-1}$). The average $I_{\text{FUV}}^{\text{diffuse}}$ versus $I_{\text{H}\alpha}$ and best-fit

line are shown in Figure 22(d). Only the data for $b > 25^\circ$ were used in the fit.

We note a very nice, unexpected, correlation between the FUV background and the diffuse H α emission, some of which is known to be emitted from the WIM. As can be seen in Figures 21 and 22, the low intensity behavior in the correlation of $I_{\text{FUV}}^{\text{diffuse}}$ with $I_{\text{H}\alpha}$ is slightly different from in the correlation with either N_{HI} or $I_{100\mu\text{m}}$. Figure 21 shows that the correlation between $I_{\text{FUV}}^{\text{diffuse}}$ and $I_{\text{H}\alpha}$ is overall straight down to the lowest intensities, while other relations become flat or curved a bit upward. Moreover, in Figure 22, at the low intensity of $I_{\text{FUV}}^{\text{diffuse}}$ ($\sim 400 - 500$ CU), the diffuse FUV intensity seems to decouple from the 100 μm intensity (and a bit from the H I column density), while the correlation between $I_{\text{FUV}}^{\text{diffuse}}$ and $I_{\text{H}\alpha}$ is still retained. These results seem to indicate that the FUV background has a stronger correlation with the H α emission, at least qualitatively, than with the other emission tracers, although the correlation coefficient between $I_{\text{FUV}}^{\text{diffuse}}$ and $I_{\text{H}\alpha}$ is not significantly higher than the other correlation coefficients (Figure 21).

Figure 23 shows the results after the removal of $\text{inverse-}\sin|b|$ dependence due to the plane-parallel medium, offering clearer evidence that the correlation between $I_{\text{FUV}}^{\text{diffuse}}$ and $I_{\text{H}\alpha}$ is stronger than other correlations. Since the far-IR emission from interstellar dust correlates well with neutral hydrogen emission (e.g., Boulanger & Pérault 1988), the diffuse FUV continuum correlates well with both $I_{100\mu\text{m}}$ and N_{HI} at the same significance, as indicated by the correlation coefficients in Figure 23(a) and (b). If the correlation between the FUV and H α backgrounds is simply due to the co-existence of dust and H α -emitting gas, the correlation of $I_{\text{FUV}}^{\text{diffuse}}$ and $I_{\text{H}\alpha}$ would have the same significance as with either $I_{100\mu\text{m}}$ or N_{HI} . On the other hand, the correlation with the H α background would be enhanced when the physical origin of a large portion of the H α background is analogous to the FUV background. We may then conjecture that the better correlation of the FUV with H α intensities is attributed to the similarity of the physical origins of the diffuse FUV and H α emissions. The fact that the correlation between $I_{\text{FUV}}^{\text{diffuse}}$ and $I_{\text{H}\alpha}$ appears to exist not only on a large scale but also in smaller-cloud scales supports the idea wherein their physical origins are at least in part related. We discuss this connection briefly in §6.1 and in more detail in a paper in preparation.

We here consider several possible explanations for the relationship between the FUV continuum and H α emissions, assuming that the physical origins of the backgrounds are indeed closely related with each other. First of all, a large fraction of the correlation between $I_{\text{FUV}}^{\text{diffuse}}$ and $I_{\text{H}\alpha}$ may be caused by the two-photon continuum emission in FUV wavelengths, which originates from the WIM. However, the contribution of two-photon emission to the FUV continuum ($I_{2\gamma}/I_{\text{H}\alpha} \approx 4 - 9\%$, as found in §6.3) is not large enough to explain the correlation relation Eq. (8).

Wood & Reynolds (1999) estimated that the scattered H α intensity at high Galactic latitudes is $\sim 5 - 20\%$ of the total H α intensity. Recently, Mattila et al. (2007) and Lehtinen et al. (2010) found that in some dust clouds, the H α radiation is mostly due to scattering by dust grains that are illuminated by a H α -emitting source off

the line of sight. Witt et al. (2010) showed that a substantial fraction of the diffuse high-latitude H α background is caused by interstellar dust scattering of H α photons that originate elsewhere in the Galaxy. In particular, they found many extended regions where the fraction of the scattered H α intensity is of an order of 50% or higher. Witt et al. (2010) and Dong & Draine (2011) also found that the most likely average fraction of scattered H α intensity is about 20% of the total H α intensity. Thus, the scattered component of the H α emission may strengthen the correlation between the diffuse H α and FUV intensities, especially at high latitudes.

It should be noted here that the differences between the data in Figure 22(b) and Figure 22(d) accord with the increasing significance of the dust-scattered H α emission with latitude. At low latitudes the diffuse H α emission is mostly from ionized gas and not related to dust-scattering, while the FUV background is from dust-scattering. Therefore, at low latitudes and high values of the diffuse FUV intensity, a much wider range of variability in the H α intensity is found for a given value of the diffuse FUV intensity (Figure 22(d)) while the diffuse FUV intensity still correlates with 100 μm emission showing an enhancement due to the effects of strong forward-scattering (see §5.1). On the other hand, at high latitudes and low values of the diffuse FUV intensity, much of the structure in the faint H α background may be due to scattering. Thus, we are seeing a linear correlation with the diffuse FUV intensity there. In other words, the H α contribution from dust-scattering becomes increasingly important at higher latitudes. Such a strong linear correlation seems to imply that a significant portion of H α at high latitudes is due to dust-scattering. A more detail comparison of the diffuse FUV and H α maps in both large and small scales is needed to address how large portion of the diffuse H α emission is due to dust-scattering.

Finally, there is one possibility beyond the scattered H α that is worth considering. The ISM may have low-density paths and voids that allow for ionizing photons from midplane OB stars to reach and ionize gas many kiloparsecs above the Galactic plane (Wood et al. 2010). Pathways that provide lower than average densities to high latitudes could enhance both scattered FUV and gas ionized by the Lyman continuum from the same OB stars that are much closer to the Galactic plane. Combined with the scattered H α emission, the presence of such pathways could provide a stronger correlated link between FUV and H α . In this regard, we note that if ionizing photons could use low-density paths to penetrate a turbulent ISM and reach high latitude clouds, such as LDN 1780, the resulting ionization would be limited to a thin outer shell and the ambient medium of the clouds (Witt et al. 2010). Wood et al. (2010) estimated that only ~ 0.05 pc thick skin of LDN 1780 would be photoionized. For such morphology, the optically thick core regions would appear relatively dark, which contradicts the observations described in Mattila et al. (2007) and Witt et al. (2010). However, we note that this does not preclude ionizing photons travelling to high latitudes. Photoionization would contribute to a portion of the H α intensity seen in LDN 1780, although dust-scattering is the dominant process for the H α intensity on the cloud. Therefore, further investigation is needed to disentangle

which process (dust-scattered H α emission versus in-situ ionized gas) is more significant in explaining the correlation between the diffuse FUV and H α emissions.

A weak saturation effect in the correlation between $I_{\text{FUV}}^{\text{diffuse}}$ and $I_{\text{H}\alpha}$, which is similar to but much weaker than those in the correlation of $I_{\text{FUV}}^{\text{diffuse}}$ versus N_{HI} and $I_{100\mu\text{m}}$, is also noticeable. The weak saturation seen in the correlation with $I_{\text{H}\alpha}$ may be easily understood through the fact that the WIM can also be approximated with a plane-parallel model but the extinction cross-section at FUV is higher than that of H α .

5.3. Correlation with Galactic Latitude

If the diffuse FUV background correlates primarily with Galactic latitude $|b|$, the FUV background intensity is described by $C_1 \csc |b| + C_2$. In addition to these, we also noted in the previous section that the diffuse FUV intensity can be approximated with a simple plane-parallel model defined by $C_1 \csc |b|$. We thus fitted the data with two trial functions, one with two free parameters and the other with only one free parameter.

The dependence on $\csc |b|$ was also obtained by averaging the diffuse FUV intensity for a given Galactic latitude. Best regression functions are then given by

$$I_{\text{FUV}}^{\text{diffuse}} = \frac{846.7 \pm 96.1}{\sin |b|} + (-457.2 \pm 100.5) \text{ CU}, \quad (9)$$

and

$$I_{\text{FUV}}^{\text{diffuse}} = \frac{412.3 \pm 10.3}{\sin |b|} \text{ CU} \quad (10)$$

for two-parameters and one-parameter models, respectively. The average intensity of the FUV background versus $|b|$ are also shown in Figure 22. The regression functions with two and one parameters are denoted by solid and dashed lines, respectively. The value of the two-parameters function at $\sin |b| = 1$ is a bit lower than the value obtained by Fix et al. (1989), but still within their error range. We note that the two-parameters model is better in explaining the dependence of $I_{\text{FUV}}^{\text{diffuse}}$ on Galactic latitude. However, the physical interpretation of the two-parameters model is problematic, as discussed in §6.4.

5.4. Comparison with the Soft X-ray

Comparison of the FUV background with the soft X-ray emission has been mentioned by Joubert et al. (1983) and Zvereva et al. (1982). Especially Zvereva et al. (1982) claimed there was a good correlation of the FUV intensity in high latitude range ($|b| > 30^\circ$) with soft X-ray brightness. They interpreted the correlation as an indication of the significant contribution of the hot ISM to the diffuse FUV background. However, Joubert et al. (1983) argued that hot gas has too small an emission measure to contribute significantly to the FUV background. Soft X-ray emission has been observed extensively with ROSAT and is well-known to be anti-correlated with H I column density. Indeed, we found a strong anti-correlation between the diffuse FUV intensity and the soft X-ray background, as shown in Figure 21(d). This anti-correlation between the diffuse FUV background and the soft X-ray also supports the dust-scattered origin of the diffuse FUV background.

6. DISCUSSION

6.1. Log-normal nature of the FUV intensity distribution?

In presenting the results, we used logarithmic scales to visualize large orders of magnitude in observed FUV intensity. Here, we show that the distribution of the diffuse FUV intensity seems to be well represented by a log-normal distribution or, equivalently, a Gaussian distribution in a logarithm scale, although its detailed study is beyond the scope of the present paper.

Hill et al. (2008) found that the histogram of the H α emission line observed from the WIM fits well with a log-normal distribution. They attributed the log-normal nature to the turbulence in the WIM. A log-normal distribution is the expected probability density function of density and/or column density for the ISM with a density structure established by turbulence (e.g., Vázquez-Semadeni & Passot 1999). Since the scattered FUV intensity is directly related to the dust column density, the log-normal property of the distribution of the diffuse FUV intensity is a natural consequence of the density structure and the turbulence property of the ISM. Thus in Figure 24, we plotted intensity histograms of $I_{\text{FUV}}^{\text{diffuse}} \sin |b|$ for various Galactic latitude ranges together with best-fit log-normal functions, and found that the intensity distributions are indeed well represented with log-normal functions. Here, we removed the Magellanic Clouds and 19 large-scale regions (the same regions as in Hill et al. 2008) with significantly enhanced H α emission to avoid discrete ionized regions where the contribution of two-photon emission to $I_{\text{FUV}}^{\text{diffuse}}$ may be significant. We also removed some high intensity “streaks” (most visible in the left panel of Figure 6(b)) that show up in the exposure maps.

Log-normal distribution shows an extended tail to large intensity values in a linear scale. Some evidence of the extended tail in an intensity histogram has already been noticed in the previous studies. Joubert et al. (1983) noted that the distributions of the points in correlations between UV brightnesses and H I column density are not symmetrical with respect to the linear regression lines. There was a high flux tail in the distribution of the UV intensities at a given value of $N(\text{H I})$. The intensity histograms in Figure 2 of Paresce et al. (1980) also show such extended tails. These regions with UV intensity excesses were rejected for the correlation studies in Joubert et al. (1983) and Péault et al. (1991) by eliminating the points in the tail with counts larger than the median by several times the dispersion and iterating the procedure. Joubert et al. (1983) attributed this property to an excess FUV radiation in certain regions of the sky, perhaps due to two photon emission by ionized gas. However, Deharveng et al. (1982) and Reynolds (1992) showed that the emission from the WIM is unlikely to contribute significantly to the general diffuse UV background. Péault et al. (1991) found that the excess in the intensity histogram does not obey the Poisson distribution; they attributed the high-count skewness and tail to the contribution of the stars brighter than $m(\text{UV}) = 8$ and unresolved faint stars. However, we argued that contribution of residual stars to the diffuse FUV background is not significant. In addition, the faint late-type stars cannot explain the hardness ratio observed at low inten-

sity regions, as shown in §4. [Schiminovich et al. \(2001\)](#) also noted a large variance in the FUV intensity and attributed the observed variance to the “cosmic variance” predicted by the multi-cloud model combined with multiple scattering and three-dimensional radiation field variance. We thus believe that the anomalous high intensity tails shown in previous studies are in fact due to an intrinsic property of the log-normal nature of the diffuse FUV background. A detailed statistical property of the dust density distribution can be investigated through a radiative transfer modeling of the starlight dust-scattered off in turbulent media.

It may also be possible to isolate high-intensity tails in the histograms and identify extended local features in the FUV maps. Some locally enhanced features were found, but bright regions generally had a patchy appearance. We also found that some of the enhanced features in the FUV sky coincided with the H α sky, but not always. We note here that the observed intensity toward a cloud could be higher, lower, or equal to its surroundings (as demonstrated in [Mattila et al. 2007](#)), depending on the scattered intensity, incident intensity from behind the cloud, and cloud optical depth. Therefore, the high-intensity tails in histograms do not necessarily correspond to local dust clouds. In addition, because of the difference in dust-extinction cross-sections at the FUV wavelengths and H α line, there would not be a strict correlation between diffuse FUV and H α emissions, even when all the FUV and H α background photons originate from dust-scattering. The origin of both the high-intensity tails in the histograms and the diffuse H α line emission may be elucidated by more detailed analyses of the dust clouds observed in both the FUV wavelengths and H α line, along with self-consistent radiative transfer models. But, such analyses are beyond the scope of the present paper.

6.2. Relative softness of the diffuse radiation

We found a weak reddening of the diffuse radiation relative to the direct starlight in §4. In order to understand the trend, we calculated the scattered to direct intensity ratio for a simplified case where a point source is embedded in a homogeneous spherical dust cloud. As noted in [Witt et al. \(1982\)](#), the analytical expression derived by [Code \(1973\)](#) approximates the scattered to the unattenuated luminosity ratio very well. In the approximation, the scattered intensity is given by

$$\frac{L_{\text{scatt}}}{L_0} = \frac{2}{(1 + \zeta) e^{\xi \tau} + (1 - \zeta) e^{-\xi \tau}} - e^{-\tau}$$

where $\zeta = \sqrt{(1 - a) / (1 - ag)}$ and $\xi = \sqrt{(1 - a)(1 - ag)}$, and the attenuated direct starlight by $L_{\text{direc}} = L_0 e^{-\tau}$. Here, the quantities L_0 , a , g , and τ refer to the unattenuated stellar luminosity, grain albedo, phase function asymmetry factor, and radial optical depth of the spherical cloud measured from the center to the outer edge.

We calculated ratios L_{direc}/L_0 , L_{scatt}/L_0 , and $L_{\text{scatt}}/L_{\text{direc}}$ as a function of wavelength using the extinction cross-section $\sigma(\lambda)$, $a(\lambda)$, and $g(\lambda)$ from [Draine \(2003\)](#) for an illustrative case of $\tau(1550 \text{ \AA}) = 2$ in Figure 25. Here, L_0 , L_{direc} , and L_{scatt} are the input, direct, and scattered luminosities. Note that the albedo $a(\lambda)$

is an increasing function with the wavelength. For comparison, we also plotted the results calculated for three hypothetical cases: (1) the case of a constant albedo of $a(1550 \text{ \AA})$ and a variable asymmetry factor $g(\lambda)$, (2) the case where both a and g are constants obtained at 1550 \AA , and (3) the case in which the wavelength-dependence of $a(\lambda)$ is reversed so that the albedo decreases with the wavelength. The figure shows that assuming the asymmetry factor to be a constant does not significantly affect the result while the albedo does. As is evident, the directly-escaped spectrum is redder or softer than the input spectrum (Figure 25a). When a constant albedo is assumed, we obtain a scattered spectrum reddened compared to the unattenuated input spectrum, but bluer than the (attenuated) directly-escaped spectrum because of the rapid increase of the absorption with the wavelength. However, as the albedo increases with the wavelength in the model of [Weingartner & Draine \(2001\)](#) and [Draine \(2003\)](#), the scattered spectra rise much more rapidly with the wavelength than the attenuation, thereby giving a relatively-red scattered spectrum compared to the directly escaped spectrum. In the case in which the wavelength-dependence of $a(\lambda)$ is reversed, the scattered spectrum become bluer relative to both the unattenuated input and the reddened directly-escaped spectra, which is contrary to the other cases. The same trend is observed when the optical depth is varied. We therefore conclude that the relative softness of the diffuse background radiation compared to the stellar radiation field is attributed to the increase of dust albedo with the wavelength.

In §4, we noticed a weak rise in the diffuse spectra longward of 1550 \AA . The rise itself tells nothing about the wavelength-dependence of dust albedo unless the incident unattenuated spectrum $I_0(\lambda)$ is known. Instead, the relative softness or hardness of the scattered radiation compared to the directly observed radiation can give direct information about the wavelength-dependence of dust albedo. In this regard, we note that the dust albedo provided by [Bruzual et al. \(1988\)](#) is constant or decreases with the wavelength in FUV, and thus is not consistent with our results. A more detailed analysis on the spectral shape can be obtained by radiative transfer models including wavelength dependence in calculating stellar radiation fields rather than that performed for a single wavelength band as have been done by [Witt et al. \(1997\)](#) and [Schiminovich et al. \(2001\)](#).

6.3. Contribution of two-photon continuum emission

The WIM, which is expected to have a temperature of $\sim 8000 \text{ K}$, must be a source of two-photon continuum in the FUV wavelengths, potentially impacting the interpretation of the FUV continuum background ([Reynolds 1992](#)). The two-photon continuum intensity at $\sim 1600 \text{ \AA}$ due to the WIM with a temperature of 8000 K is estimated to be $I_{2\gamma} = 57.4(I_{\text{H}\alpha}/R) \text{ CU}$ ([Reynolds 1990, 1992](#); see also Figure 26). Using the average H α intensity distribution $I_{\text{H}\alpha} \approx 1.2 \text{ csc}|b| \text{ R}$, which was obtained from rather limited observations, Reynolds also obtained $I_{2\gamma} \approx 70 \text{ csc}|b| \text{ CU}$. However, using the result of [Hill et al. \(2008\)](#) obtained from the full WIM observations, the distribution of H α for $|b| \geq 10^\circ$ is fitted on average by $I_{\text{H}\alpha} \approx 0.625 \text{ csc}|b| \text{ R}$ (see also [Dong & Draine](#)

2011). This leads to a lower two-photon intensity of $I_{2\gamma} \approx 36 \csc|b|$ CU, which accounts for $\sim 9\%$ of the FUV background (Eq. 10).

The two-photon continuum's contribution to the diffuse FUV intensity is reduced even further when the model of WIM developed by Dong & Draine (2011) is adopted. Recent observations using the *Wilkinson Microwave Anisotropy Probe* (*WMAP*) have found that the ratio of the free-free radio continuum to $\text{H}\alpha$ is surprisingly low in the WIM (Davies et al. 2006; Dobler & Finkbeiner 2008; Dobler, Draine, & Finkbeiner 2009). Dong & Draine (2011) considered a three-component model consisting of a mix of (1) photoionized hot gas, (2) gas that is recombining and cooling after removal of a photoionizing source, and (3) cool H I gas. In their standard model for explaining the observed intensity ratios of the free-free radio continuum to $\text{H}\alpha$ and [N II] $\lambda\lambda 6583$ to $\text{H}\alpha$, the authors assumed that the scattered fraction of the $\text{H}\alpha$ originating from the hot gas is $f_{\text{H}\alpha}^{(\text{refl})} = 0.2$, while the fractions of the hot, cooling, and H I gases are $f_{\text{H}\alpha}^{(\text{hot})} = 0.22$, $f_{\text{H}\alpha}^{(\text{cooling})} = 0.56$, and $f_{\text{H}\alpha}^{(\text{HI})} = 0.02$, respectively. The temperature of the hot gas was found to be $T^{(\text{hot})} = 9100$ K. The cooling gas cooled down rapidly from its initial temperature $T^{(\text{cooling})} \sim 10,000$ K to ~ 400 K (Fig. 3 of Dong & Draine 2011).

Using the two-photon spectral profile (Kwok 2007), the hydrogen recombination coefficient α_{2S} for case B (Table 3 of Martin 1998), and the $\text{H}\alpha$ emission rate (Eq. 10 of Dong & Draine 2011), we estimated the two-photon intensity averaged over 1370–1710 Å from hot and cooling ionized gas (Figure 26): $I_{2\gamma}^{(\text{hot})} = 59.1(I_{\text{H}\alpha}/R)$ CU, and $I_{2\gamma}^{(\text{cooling})} = 26.0(I_{\text{H}\alpha}/R)$ CU. The two-photon intensity of the cooling gas is mostly determined by the gas with a temperature of 400 K, because the cooling gas is 400 K or lower for more than 98% of its lifetime (Fig. 3 of Dong & Draine 2011). The total two-photon intensity originating from the ionized gas is then given by $I_{2\gamma} = f_{\text{H}\alpha}^{(\text{cooling})} I_{2\gamma}^{(\text{cooling})} + f_{\text{H}\alpha}^{(\text{hot})} I_{2\gamma}^{(\text{hot})} = 28.4(I_{\text{H}\alpha}/R)$ CU. The distribution of two-photon emission is then $I_{2\gamma} \approx 18 \csc|b|$ CU, corresponding to $\sim 4\%$ of the FUV background intensity.

In summary, two-photon emission may account for ~ 4 – 9% of the diffuse FUV background. Although the two-photon emission may be significant in discrete bright H II regions, the contribution of two-photon emission to the diffuse FUV background is much smaller than has previously been suggested. The large variation of $I_{\text{FUV}}^{\text{diffuse}}$ (from a factor of 2–3 up to an order of magnitude) is also unlikely to be the result of two-photon emission.

6.4. Isotropic component

The phrase “isotropic component” has been used to refer to the diffuse intensity extrapolated to $N_{\text{HI}} = 0$, or, alternatively, to $|b| = 90^\circ$, and is frequently assumed to be extragalactic background. Wright (1992) claimed that the isotropic extragalactic component of the diffuse FUV background should be obtained by extrapolating to $\csc(|b|) = 0$, instead of to $\csc|b| = 1$ as practiced by Fix et al. (1989). Witt & Petersohn (1994) discussed systematic errors arising in the method of extrapolat-

ing high latitude measurements of the diffuse FUV background to $N_{\text{HI}} = 0$ or to $\csc(|b|) = 0$ to derive the level of the cosmic extragalactic background. They argue that the derivation of the cosmic background from the extrapolation of the diffuse FUV background to $N_{\text{HI}} = 0$ is more likely to yield a reliable result. They found, in fact, that extrapolations of the predicted FUV background intensities through a Monte-Carlo radiative transfer model to $\csc|b| = 0$ produce negative values when it should produce a zero intercept. We also found from the SPEAR data that the extrapolation to $\csc|b| = 0$ indeed produces a negative value of ~ -400 CU.

A discussion of the origin of the isotropic component is beyond the scope of the present paper. Onaka & Kodaira (1991) observed intensities as low as 300 CU at high Galactic latitudes. Schiminovich et al. (2001) placed constraints on the extragalactic background 200 ± 100 CU. We also found the isotropic component consistent with previous authors, but a bit higher. It should be noted that a similar level of the isotropic component was found from the relationship between the diffuse FUV and $\text{H}\alpha$ emissions (Eq. 8). However, it is not clear at this time that all of the ~ 300 CU, the extrapolation value of the average FUV- N_{HI} correlation to $N_{\text{HI}} = 0$, corresponds to the extragalactic background. In fact, we observed the FUV intensities lower than 300 CU as is obvious in Figure 4. Witt et al. (1997) analyzed the FUV data observed in the FAUST experiment (Bowyer et al. 1993) and estimated a contribution of about 700 ± 200 CU that is uncorrelated with Galactic parameters. They argued that the extragalactic component of more than 300 CU is excluded by the lower limit directly measured by Onaka & Kodaira (1991) and concluded that most likely value of isotropic extragalactic background radiation would be 160 ± 50 CU, after correction for Galactic extinction.

7. SUMMARY

In this paper, we reported some general results on the diffuse FUV background and the total FUV radiation observed with SPEAR/FIMS. Our main conclusions are as follows:

1. Strong anisotropies are found in not only the diffuse background intensity but also in the hardness ratio (1370–1520 Å to 1560–1710 Å).
2. We found a good correlation between the diffuse FUV background and other Galactic quantities, such as H I column density, 100 μm emission, and $\text{H}\alpha$ emission. The correlation of the FUV continuum background with the diffuse $\text{H}\alpha$ emission seems to be better than with the other quantities. Anti-correlation with the soft X-ray was also found. Correlation of the FUV background with the direct stellar intensity is rather weaker than the correlation with other waveband observations, such as 100 μm and $\text{H}\alpha$ emissions.
3. The fact that a linear correlation of the FUV background with the diffuse $\text{H}\alpha$ emission is found at low intensities seems to indicate that the dust-scattered component of $\text{H}\alpha$ becomes increasingly important at higher latitudes.

4. The spatially-averaged total FUV intensity, including the direct stellar and diffuse FUV intensities, observed with SPEAR/FIMS is weaker than the well-known ISRF models, such as the Habing, Mathis, and Draine models.
5. The spectrum of the diffuse FUV background is in general flat and a bit softer than the directly-escaped stellar spectrum. The relative softening can be attributed to the rise of dust albedo as the wavelength increases.
6. The hardness ratio seems to follow in general the longitudinal distribution of OB-type stars in the Galactic plane.
7. The “isotropic component” obtained by comparing the FUV background with other ISM tracers, N_{HI} , $100 \mu\text{m}$, and $\text{H}\alpha$ emissions is consistent with the previous results.
8. Evidence that the intensity histogram of the diffuse background is well represented by log-normal distribution is found, as for the diffuse $\text{H}\alpha$ emission.

The above results well accord with the fact that most of the diffuse FUV background is scattered light of the

FUV stellar radiation by the interstellar dust. Witt et al. (1997) and Schiminovich et al. (2001) developed radiative transfer models to interpret the diffuse FUV background. Our future work will deal with a Monte-Carlo simulation model incorporating three-dimensional stellar distribution obtained from the *Hipparcos* catalog and three-dimensional dust distributions modeled by several authors such as Drimmel & Spergel (2001) and Drimmel et al. (2003). The model compared with the SPEAR/FIMS data should provide a better understanding to the observational results.

The SPEAR/FIMS was supported by NASA grant NAG5-5355 and flew on the STSAT-1 Mission, supported of the Korea Ministry of Science and Technology. We acknowledge the use of the Legacy Archive for Microwave Background Data Analysis (LAMBDA). Support for LAMBDA is provided by the NASA Office of Space Science. K.-I. S. was supported by a National Research Foundation of Korea grant funded by the Korean government (grant no. 313-2008-2-C00377). We thank the anonymous referee for comments that led to improvements in the manuscript.

REFERENCES

Anderson, R. C., Brune, W. H., Henry, R. C., Feldman, P. D., & Fastie, W. G. 1979, ApJ, 233, L39

Arenou, F., Grenon, M., & Gómez, A. 1992, A&A, 258, 104

Bessell, M. S., Castelli, F., & Plez, B. 1998, A&A, 333, 231

Bohlin, R. C., Savage, B. D., & Drake, J. F. 1978, ApJ, 224, 132

Boulaenger, F., & Pérault, M. 1988 ApJ, 330, 964

Bowyer, S. 1991, ARA&A, 29, 59

Bowyer, S., Sasseen, T., Lampton, M., & Wu, X. 1993, ApJ, 415, 875

Bruzual, A. G., Magrid, G., & Calvet, N. 1988, ApJ, 333, 673

Castelli, F., Kurucz, R. L. 2003, IAUS, 210, 20

Chen, B., Vergely, J. L., Valette, B., & Carraro, G., 1998, A&A, 336, 137

Code, A. D. 1973, in *IAU Symposium 52, Interstellar Dust and Related Topics*, ed J. M. Greenberg and H. C. van de Hulst, (Dordrecht: Reidel), p. 505

Cox, D. P., & Reynolds, R. J. 1987, ARA&A, 25, 303

Dame, T. M., & Thaddeus, P. 1985, ApJ, 297, 751

Davies, R. D., Dickinson, C., Banday, et al. 2006, MNRAS, 370, 1125

Deharveng, J. M., Joubert, M., & Barge, P. 1982, A&A, 109, 179

Dickey, J. M., & Lockman, F. J. 1990, ARA&A, 28, 215

Dobler, G., Draine, B., & Finkbeiner, D. P. 2009, ApJ, 699, 1374

Dobler, G., & Finkbeiner, D. P. 2008, ApJ, 680, 1235

Dong, R., & Draine, B. T. 2011, ApJ, 727, 35

Duley, W. W., & Williams, D. A. 1980, ApJ, 242, L179

Draine, B. T. 1978, ApJS, 36, 595

Draine, B. T. 2003, ApJ, 598, 1017

Drimmel, R., & Spergel, D. N. 2001, ApJ, 556, 181

Drimmel, R., Cabrera-Lavers, & Lopez-Corredoira, M. 2003, A&A, 406, 205

Edelstein, J., Min, K.-W., Han, W., et al. 2006a, ApJ, 644, L153

Edelstein, J., Korpela, E. J., Adolfo, J., et al. 2006b, ApJ, 644, L159

Elias, F., Cabrera-Caño, J., & Alfaro, E. J. 2006, AJ, 131, 2700

Fix, J. D., Craven, J. D., & Frank, L. A. 1989, ApJ, 345, 203

Finkbeiner, D. P. 2003, ApJS, 146, 407

Gondhalekar, P. M., Phillips, A. P., & Wilson, R. 1980, A&A, 85, 272

Górski, K. M., Hivon, E., Banday, A. J., et al. 2005, ApJ, 622, 759

Habing, H. J. 1968, BAN, 19, 421

Haffner, L. M., Reynolds, R. J., Tufte, S. L., et al. 2003, ApJS, 149, 405

Haikala, L. K., Mattila, K., Bowyer, S., et al. 1995, ApJ, 443, L33

Henry, R. C. 1977, ApJS, 33, 451

Henry, R. C., Swandic, J. R., Shulman, S. D., Fritz, G. 1977, ApJ, 212, 707

Henry, R. C., Feldman, P. D., Fastie, W. G., & Weinstein, A. 1978, ApJ, 223, 437

Henry, R. C., Anderson, R. C., & Fastie, W. G. 1980, ApJ, 239, 859

Henry, R. C. 1991, ARA&A, 29, 89

Henry, R. C., & Murthy, J. 1993, ApJ, 418, L17

Henry, R. C. 2002, ApJ, 570, 697

Hill, A. S., Benjamin, R. A., Kowal, G., et al. 2008, ApJ, 686, 363

Hua, C. T., Cruvellier, P., Courtés, G., et al. 1979, In *COSPAR Proc. X-ray Astronomy* (Oxford: Pergamon Press), p. 551

Hurwitz, M., Bowyer, S., & Martin, C. 1991, ApJ, 372, 167

Jakobsen, P. 1982, A&A, 106, 375

Jakobsen, P., & Paresce, F. 1981, A&A, 96, 23

Jakobsen, P., Bowyer, S., Kimble, R., et al. 1984, A&A, 139, 481

Jakobsen, P., de Vries, J. S., & Paresce, F. 1987, A&A, 183, 335

Joubert, M., Masnou, J. L., Lequeux, J., Deharveng, J. M., & Cruvellier, P. 1983, A&A, 128, 114

Joshi, Y. C., 2005, MNRAS, 362, 1259

Kalberla, P. M. W., Burton, W. B., Hartmann, D., et al. 2005, A&A, 440, 775

Kim, I.-J., Min, K.-W., Seon, K.-I., et al. 2007, ApJ, 665, L139

Kim, I.-J., Min, K.-W., Seon, K.-I., Han, W., & Edelstein, J. 2010, ApJ, 709, 823

Kim, I.-J., Seon, K.-I., Min, K.-W., et al. 2010, ApJ, 722, 388

Korpela, E. J., Edelstein, J., Kregenow, J., et al. 2006, ApJ, 644, L163

Kregenow, J., Edelstein, J., Korpela, E. J., et al. 2006, ApJ, 644, L167

Kregenow, J. Ph. D. Thesis, University of California, 2007 (available in http://spear.ssl.berkeley.edu/papers/kregenow_thesis.pdf)

Kwok, S. 2007, Physics and Chemistry of the Interstellar Medium (Sausalito, CA: Univ. Science Books)

Lallemand, R., Welsh, B. Y., Vergely, J. L., Crifo, F., & Sfeir, D. 2003, A&A, 411, 447

Lee, D.-H., Yuk, I.-S., Jin, H., et al. 2006, ApJ, 644, L81

Lee, D.-H., Seon, K.-I., Min, K.-W., et al. 2008, ApJ, 686, 1155

Lehtinen, K., Juvela, M., & Mattila, K. 2010, A&A, 517, 79

Lequeux, J. 1990, in The galactic and extragalactic background radiation, IAU Symposium No. 139, eds. S. Bowyer, C. Leinert, Kluwer, Dordrecht, p. 185

Martin, P. G. 1988, *ApJS*, 66, 125

Martin, C., Bowyer, S. 1990, *ApJ*, 350, 242

Martin, C., Hurwitz, M., & Bowyer, S. 1990, *ApJ*, 354, 220

Mathis, J. S., Mezger, P. G., & Panagia, N. 1983, *A&A*, 128, 212

Mattila, K., Juvela, M., & Lehtinen, K. 2007, *ApJ*, 654, 131

Maucherat-Joubert, M., Cruvellier, P., & Deharveng, J. M. 1978, *A&A*, 70, 467

Maucherat-Joubert, M., Deharveng, J. M., & Cruvellier, P. 1980, *A&A*, 88, 323

Murthy, J., Henry, R. C., Feldman, P. D., & Tennyson, P. D. 1989, *ApJ*, 336, 954

Murthy, J., Henry, R. C., Feldman, P. D., & Tennyson, P. D. 1990, *A&A*, 231, 187

Murthy, J., Henry, R. C., & Sujatha, N. V. 2010, *ApJ*, 724, 1389

Murthy, J., & Henry, R. C. 2011, *ApJ*, 734, 13

Nandy, K., Thompson, G. I., Carnochan, D. J., Wilson, R. 1978, *MNRAS*, 184, 733

Nishikida, K., Edelstein, J., Korpela, E. J., et al. 2006, *ApJ*, 644, L171

Onaka, T., & Kodaira, K. 1991, *ApJ*, 379, 532

Paresce, F., & Jakobsen, P. 1980, *Nature*, 288, 119

Paresce, F., McKee, C. F., & Bowyer, S. 1980, *ApJ*, 240, 387

Park, J.-W., Min, K.-W., Seon, K.-I., et al. 2007, *ApJ*, 665, L39

Park, S.-J., Min, K.-W., Seon, K.-I., et al. 2009, *ApJ*, 700, 155

Park, J.-W., Min, K.-W., Seon, K.-I., Han, W., & Edelstein, J. 2010, *ApJ*, 719, 1964

Péroult, M., Lequeux, J., Hanus, M., & Joubert, M. 1991, *A&A*, 246, 243

Perryman, M. A. C., Lindegren, L., Kovalevsky, J., et al. 1997, *A&A*, 323, L49

Press, W. H., Flannery, B. P., Teukolsky, S. A., & Vetterling, W. T. 1992, Numerical Recipes: The Art of Scientific Computing 2nd ed. (New York: Cambridge University Press), p660

Reynolds, R. J. 1984, *ApJ*, 282, 191

Reynolds, R. J. 1985, *AJ*, 90, 92

Reynolds, R. J. 1990, The Galactic and Extragalactic Background Radiation (IAU Symp. 139), ed. S. Bowyer & C. Leinert (Dordrecht: Kluwer), 157

Reynolds, R. J. 1992, *ApJ*, 392, L35

Ryu, K., Min, K.-W., Park, J.-W., et al. 2006, *ApJ*, 644, L181

Ryu, K., Min, K.-W., Seon, K.-I., et al. 2008, *ApJ*, 678, L29

Sasseen, T. P., Lampton, M., Bowyer, S., & Wu, X. 1995, *ApJ*, 447, 630

Sasseen, T. P., Deharveng, J.-M. 1996, *ApJ*, 469, 691

Schiminovich, D., Friedman, P. G., Martin, C., & Morrissey, P. F. 2001, *ApJ*, 563, L161

Schlegel, D. J., Finkbeiner, D. P., & Davis, M. 1998, *ApJ*, 500, 525

Seon, K.-I., Han, W., Nam, U.-W., et al. 2006, *ApJ*, 644, L175

Shinn, J.-H., Min, K. W., Lee, C.-N., et al. 2006, *ApJ*, 644, L189

Shinn, J.-H., Min, K. W., Sankrit, R., et al. 2007, *ApJ*, 670, 1132

Snowden, S. L., Egger, R., Freyberg, M. J., et al. 1997, *ApJ*, 485, 125

Stothers, R., & Frogel, J. A. 1974, *AJ*, 79, 456

Straizys, V., & Kuriliene, G. 1981, *Ap&SS*, 80, 353

Straizys, V., K. Černis, & Bartašiūtė, S. 2003, *A&A*, 405, 585

Sujatha, N. V., Chakraborty, P., Murthy, J., & Henry, R. C. 2004, *BASI*, 32, 151

Tennyson, P. D., Henry, R. C., Feldman, P. D., & Hartig, G. F. 1988, *ApJ*, 330, 435

Thompson, G. I., Nandy, K., Jamar, C., et al. 1978, Catalogue of Stellar Ultraviolet Fluxes (London: Sci. Res. Council)

Van Leeuwen, F. 2007, *A&A*, 474, 653

Vázquez-Semadeni, E. & Passot, T. 1999, in Interstellar Turbulence, ed. J. Franco & A. Carramiñana (Cambridge University Press), 223

Verner, D. A., & Yakovlev, D. G. 1995, *A&AS*, 109, 125

Weller, C. 1983, *ApJ*, 268, 899

Witt, A. N., Friedmann, B. C., & Sasseen, T. P. 1997, *ApJ*, 481, 809

Witt, A. N., Walker, G. A. H., Bohlin, R. C., & Stecher, T. P. 1982, *ApJ*, 261, 492

Witt, A. N., & Petersohn, J. K. 1994, in ASP Conf. Ser., 58, The First Symposium on the Infrared Cirrus and Diffuse Interstellar Clouds, ed. R. M. Cutri & W. B. Latter (San Francisco: ASP), 91

Witt, A. N., Mandel, S., Sell, P. H., Dixon, T., & Vrijh, U. P. 2008, *ApJ*, 679, 497

Witt, A. N., Gold, B., Barness III, F. S., et al. 2010, *ApJ*, 724, 1551

Weingartner, J. C., Draine, B. T., 2001, *ApJ*, 548, 296

Welsh, B. Y., Edelstein, J., Korpela, E. J., et al. 2007, *A&A*, 472, 509

Wood, K., & Reynolds, R. J. 1999, *ApJ*, 525, 799

Wood, K., Hill, A. S., Joung, M. R., et al. 2010, *ApJ*, 721, 1387

Wright, E. L. 1992, *ApJ*, 391, 34

Zvereva, A. M., Severny, A. B., Granitzky, L. V., et al. 1982, *A&A*, 116, 312

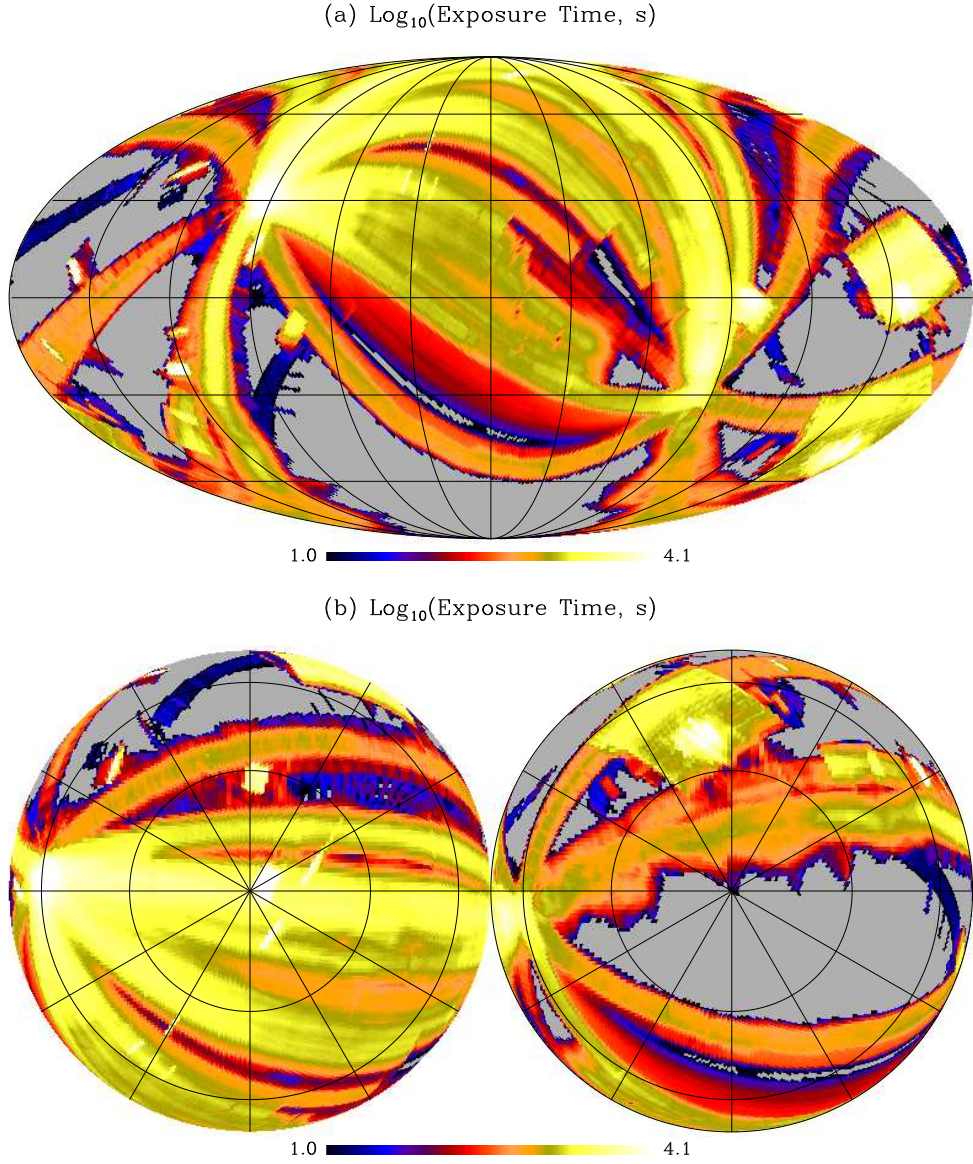


FIG. 1.— (a) Mollweide and (b) orthographic projections of sky exposure for the SPEAR/FIMS L-band observations. The map was made using the *HEALPix* scheme with $\sim 1^\circ$ pixels ($N_{\text{side}} = 64$). The intensity scales are logarithmic across the color bars. Exposure time observed with both 100% and 10% shutter apertures are combined. (a) Galactic coordinates centered at $(l, b) = (0^\circ, 0^\circ)$ with the longitude increasing toward the left are shown with latitude and longitude lines on a 30° grid. (b) The left and right sides of orthographic projections are centered at the northern and southern Galactic polar caps, respectively, and their longitude increases clockwise and counter-clockwise, respectively. In both projections, $l = 0^\circ$ is at the six o'clock position.

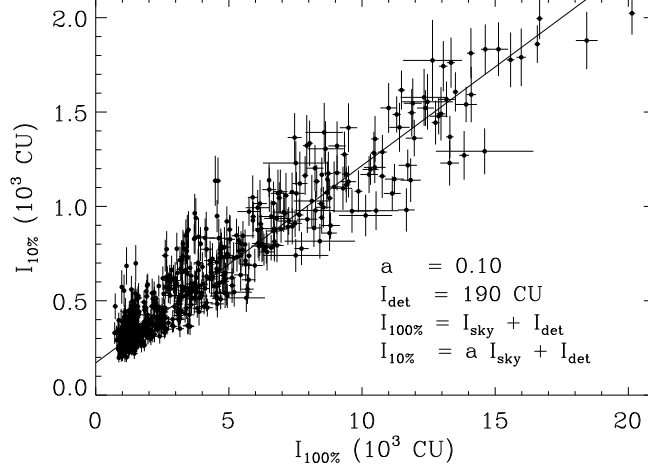


FIG. 2.— Pixel by pixel comparison of the 100% and 10% shutter aperture data. By fitting the data with a linear function, the scale factor for the 10% shutter aperture data and detector background rate are estimated. The comparison is made with the $N_{\text{side}} = 64$ maps. Here, CU represents the continuum unit (photons $\text{cm}^{-2} \text{s}^{-1} \text{\AA}^{-1} \text{sr}^{-1}$ CU).

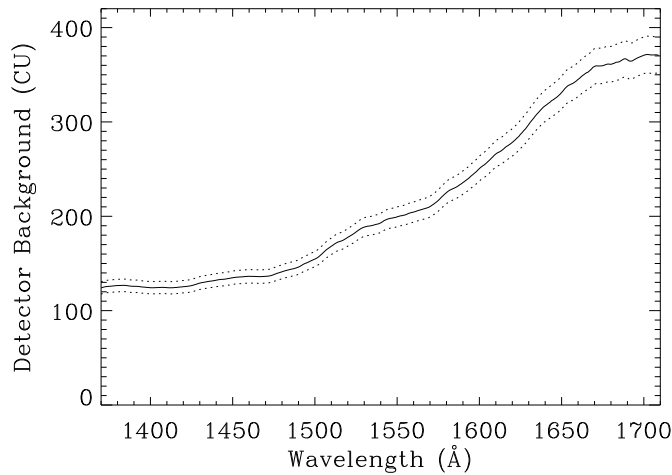


FIG. 3.— Instrumental background spectrum. The spectrum is essentially the inverse of the effective area curves, as shown in Edelstein et al. (2006b). An 1σ error range for the average of detector background value is also shown with dotted lines.

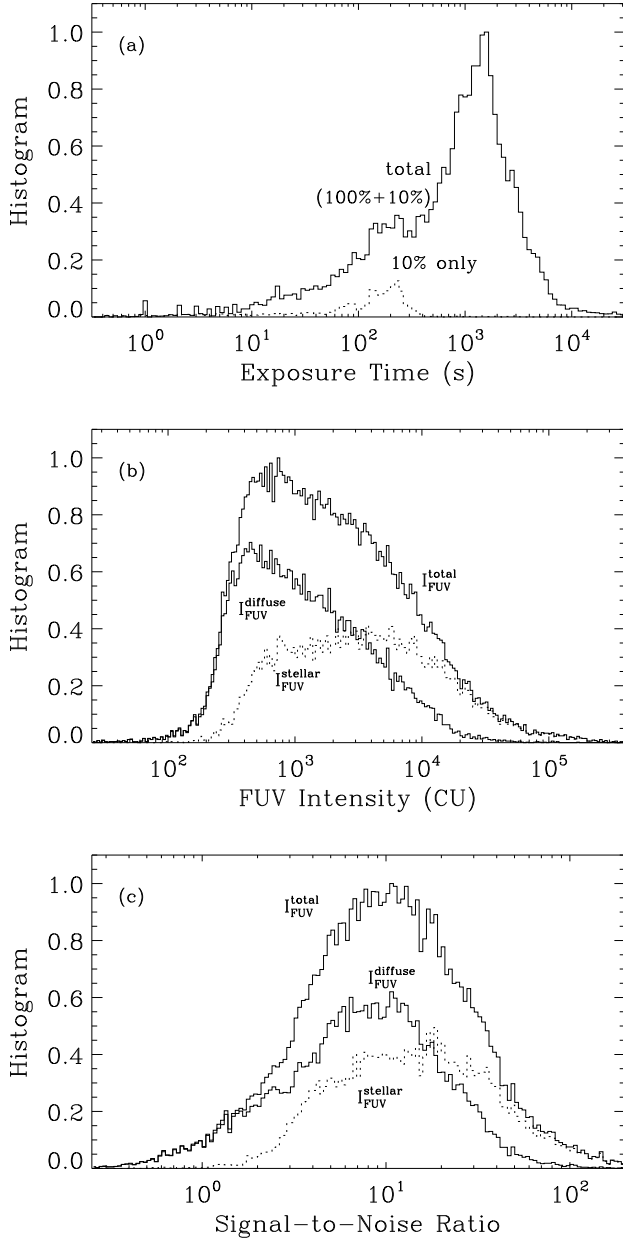


FIG. 4.— Histograms of (a) exposure time (s), (b) the FUV intensity ($\text{photons s}^{-1} \text{cm}^{-2} \text{sr}^{-1} \text{\AA}^{-1}$, CU) over the observed sky, and (c) signal-to-noise ratio with bins scaled logarithmically. The histograms are made with about 1° pixels ($N_{\text{side}} = 64$). A background of 190 CU was removed from the data to take into account the instrumental dark background.

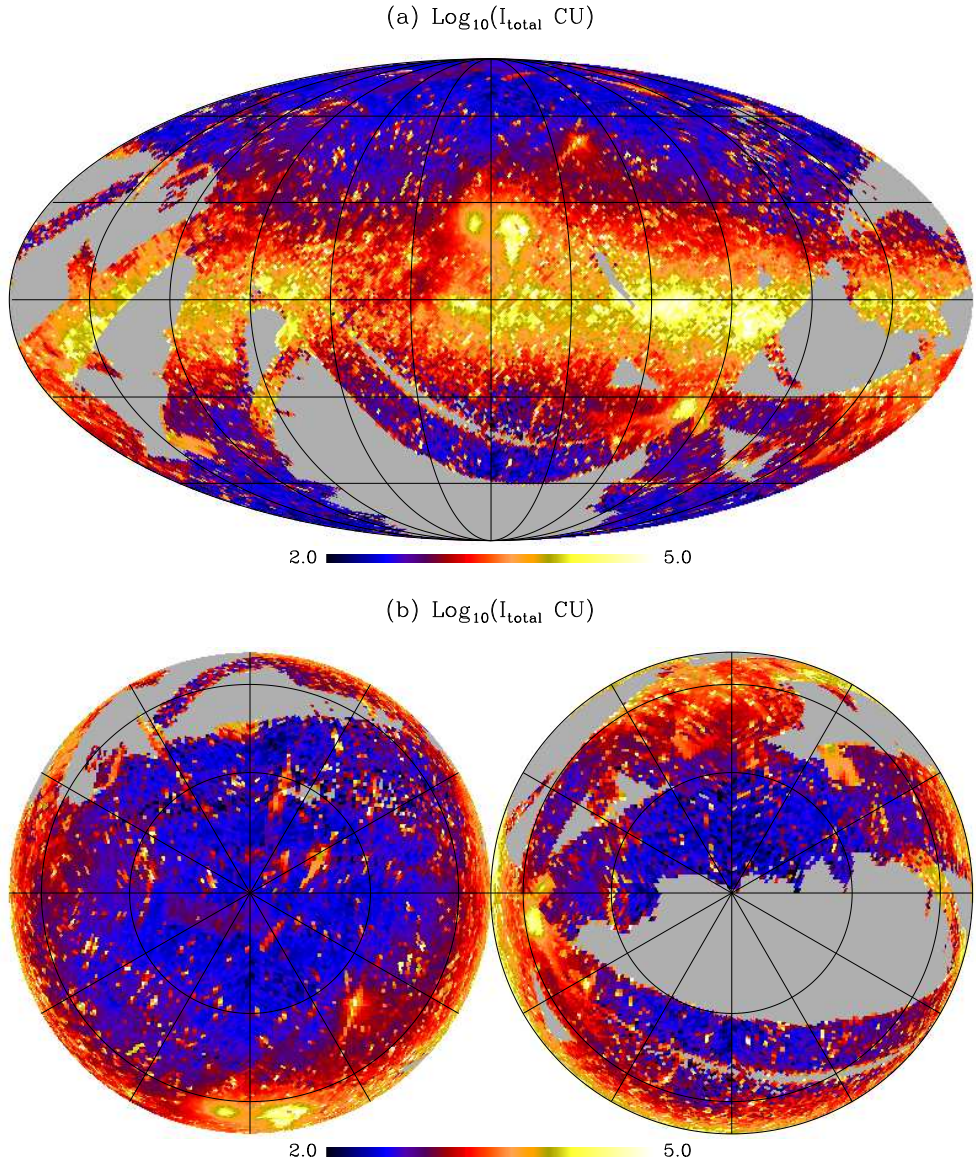


FIG. 5.— (a) Mollweide and (b) orthographic projections of the combined total (diffuse + direct stellar) FUV map observed with SPEAR/FIMS, after removal of the instrumental background. The left and right sides of orthographic projections are centered at the northern and southern Galactic polar caps, respectively, and their longitude increases clockwise and counter-clockwise, respectively. In both projections, $l = 0^\circ$ is at the six o'clock position. The intensity scales are logarithmic across the color bars.

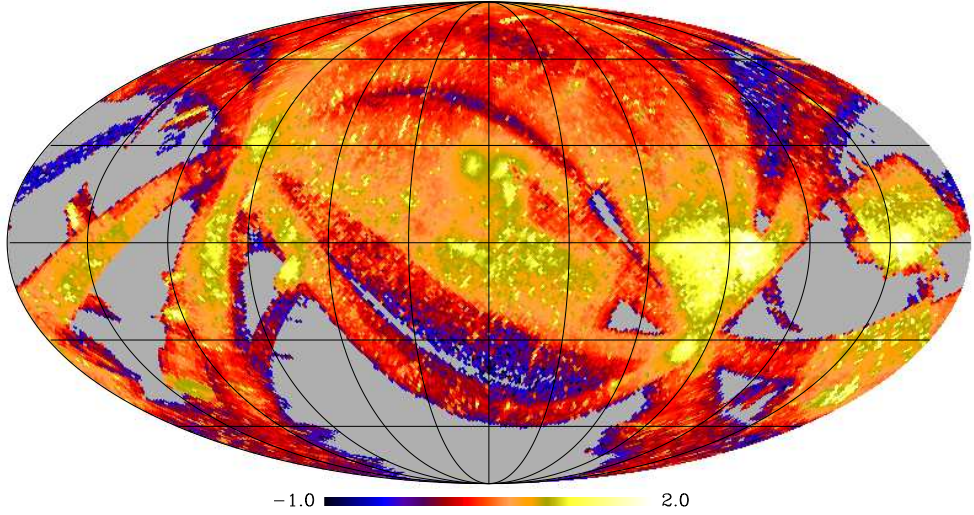
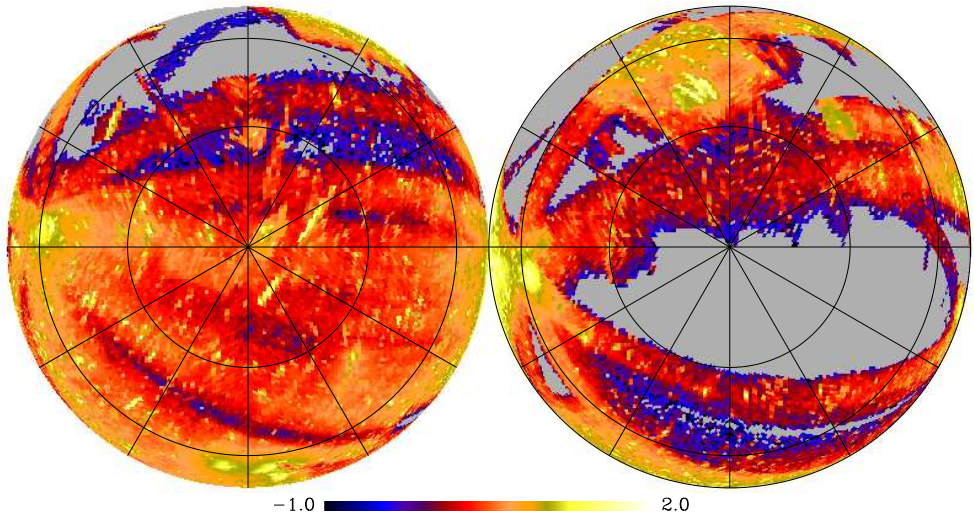
(c) $\log_{10}([\text{S}/\text{N}]_{\text{total}}/3)$ (d) $\log_{10}([\text{S}/\text{N}]_{\text{total}}/3)$ 

FIG. 5.— (c) mollweide and (d) orthographic projections of signal-to-noise ratio of the total FUV map. The left and right sides of orthographic projections are centered at the northern and southern Galactic polar caps, respectively, and their longitude increases clockwise and counter-clockwise, respectively. In both projections, $l = 0^\circ$ is at the six o'clock position. The intensity scales are logarithmic across the color bars.

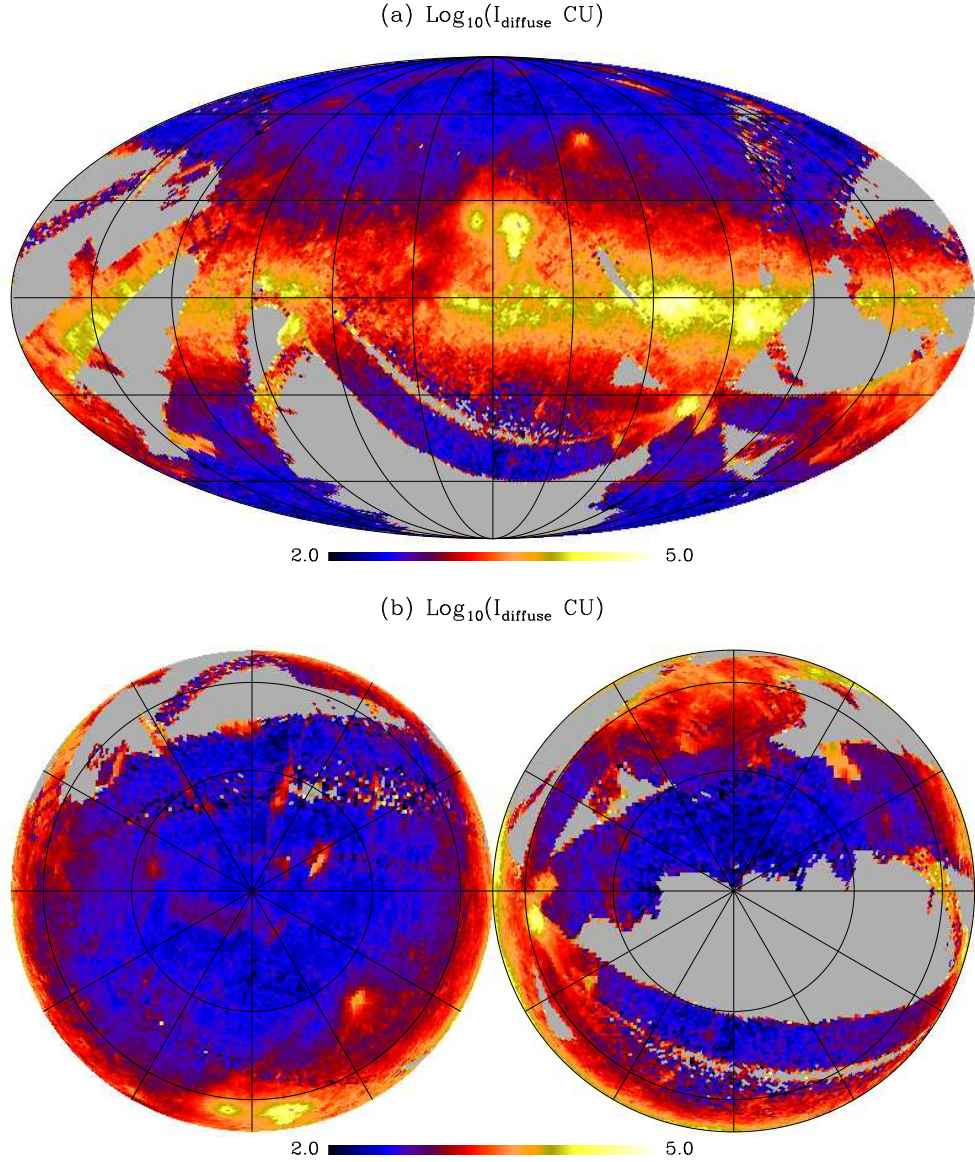


FIG. 6.— (a) Mollweide and (b) orthographic projections of the diffuse FUV background map observed with SPEAR/FIMS, after removal of locally intense pixels (stars) and the instrumental background. The left and right sides of orthographic projections are centered at the northern and southern Galactic polar caps, respectively, and their longitude increases clockwise and counter-clockwise, respectively. In both projections, $l = 0^\circ$ is at the six o'clock position. The intensity scales are logarithmic across the color bars.

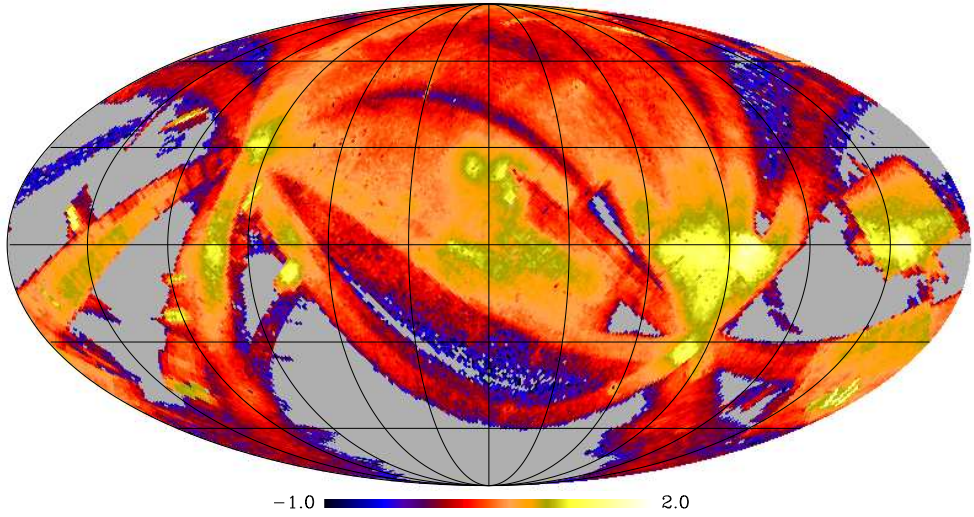
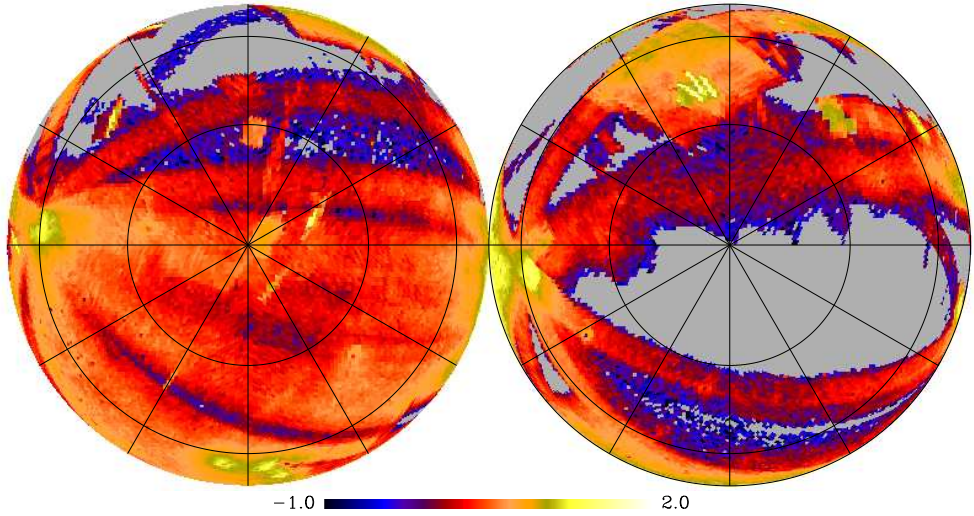
(c) $\log_{10}([S/N]_{\text{diffuse}}/3)$ (d) $\log_{10}([S/N]_{\text{diffuse}}/3)$ 

FIG. 6.— (c) mollweide and (d) orthographic projections of signal-to-noise ratio of the diffuse FUV map. The left and right sides of orthographic projections are centered at the northern and southern Galactic polar caps, respectively, and their longitude increases clockwise and counter-clockwise, respectively. In both projections, $l = 0^\circ$ is at the six o'clock position. The intensity scales are logarithmic across the color bars.

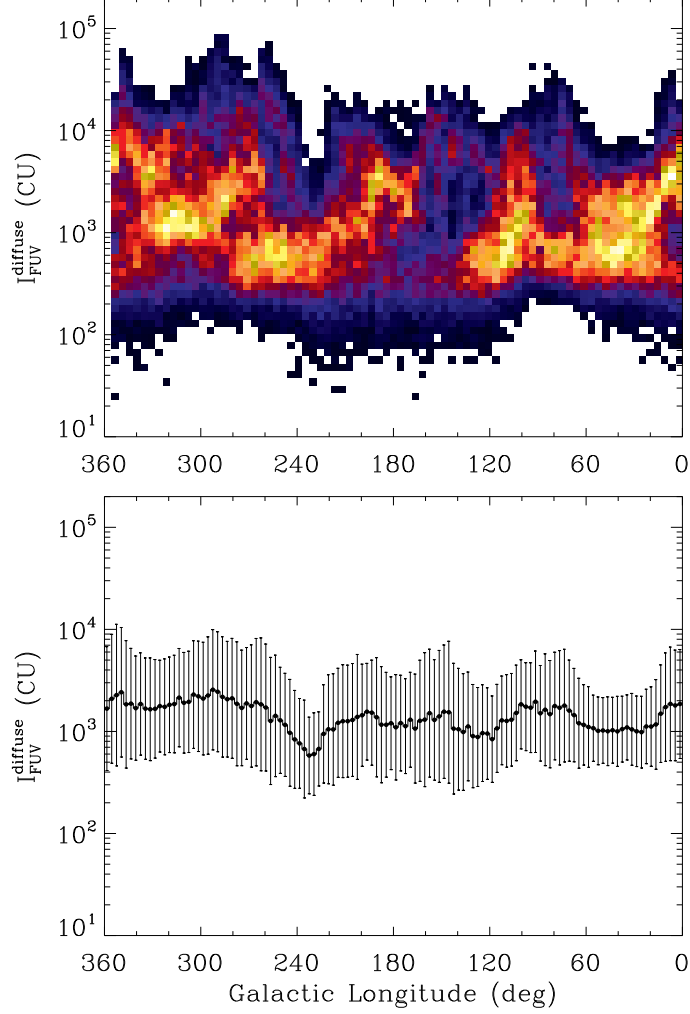


FIG. 7.— The diffuse FUV intensity versus Galactic longitude. The top panel plots the two-dimensional histogram of the diffuse FUV intensity as a function of Galactic longitude. The bottom panel plots the median value within each of the 3° longitude strips from the data. The vertical extent of each plotted bar is determined from the average deviation about the median within that bin.

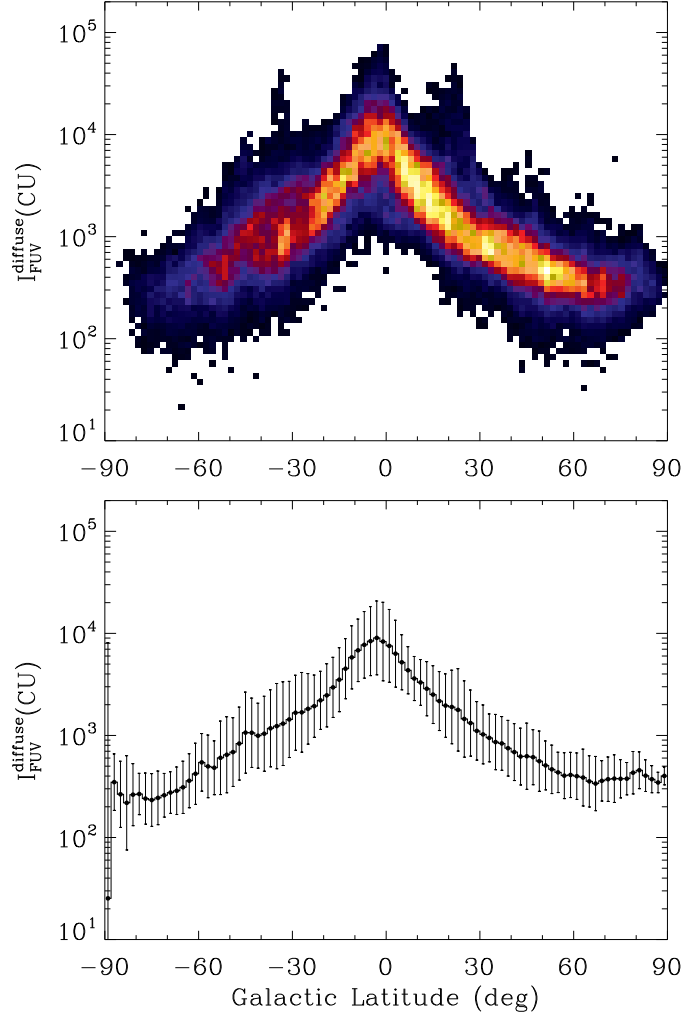


FIG. 8.— The diffuse FUV intensity versus Galactic latitude. The top panel plots the two-dimensional histogram of the diffuse FUV intensity as a function of Galactic latitude. The bottom panel plots the median value within each of the 2° latitude strips from the data. The vertical extent of each plotted bar is determined from the average deviation about the median within that bin.

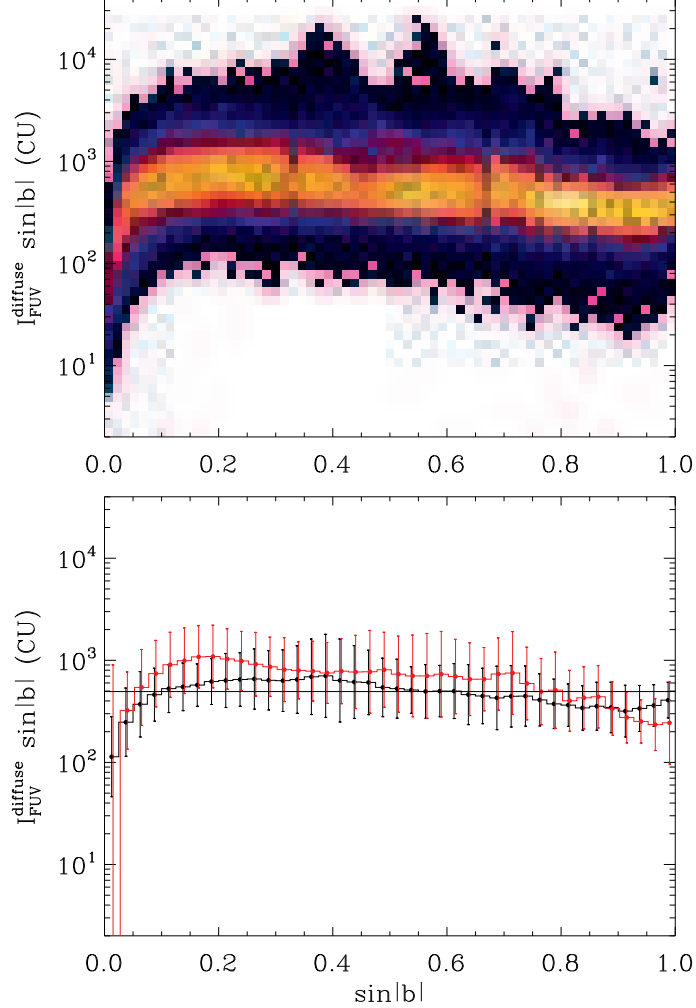


FIG. 9.— $I_{\text{FUV}}^{\text{diffuse}} \sin|b|$ versus $\sin|b|$. The top panel plots the two-dimensional histogram as a function of Galactic longitude. The bottom panel plots the median value within each of the $\Delta \sin|b| = 0.025$ latitude strips from the data. The vertical extent of each plotted bar is determined from the average deviation about the median within that bin. The black and red points represent the data observed toward northern and southern Galactic latitude, respectively. The horizontal line denotes the median $I_{\text{FUV}} \sin|b|$ value.

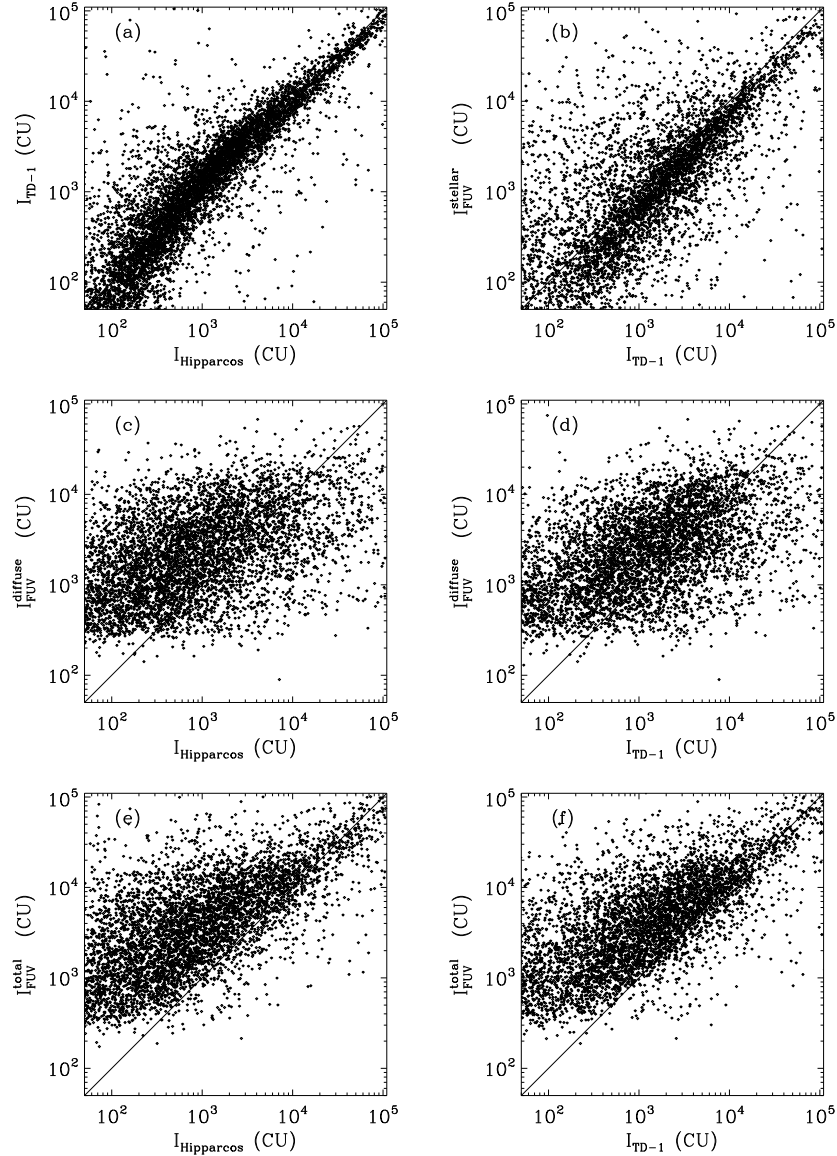


FIG. 10.— Comparison between the TD-1 stellar equivalent diffuse intensity (SEDI), the *Hipparcos* SEDI, and the SPEAR/FIMS intensities. (a) The TD-1 SEDI versus the *Hipparcos* SEDI, (b) the direct stellar intensity observed with SPEAR/FIMS versus the TD-1 SEDI, (c) the diffuse FUV background versus the *Hipparcos* SEDI, (d) the diffuse FUV background versus the TD-1 SEDI, (e) the total (direct stellar + diffuse) FUV intensity versus the *Hipparcos* SEDI, and (f) the total FUV intensity versus the TD-1 SEDI. Here, the resolution parameter $N_{\text{side}} = 32$ corresponding to angular resolution of $\sim 1.8^\circ$ is used. The TD-1 SEDI was estimated using the 1565 Å band, and the others were calculated over the same wavelength bands 1370–1520, 1560–1660, and 1680–1720 Å.

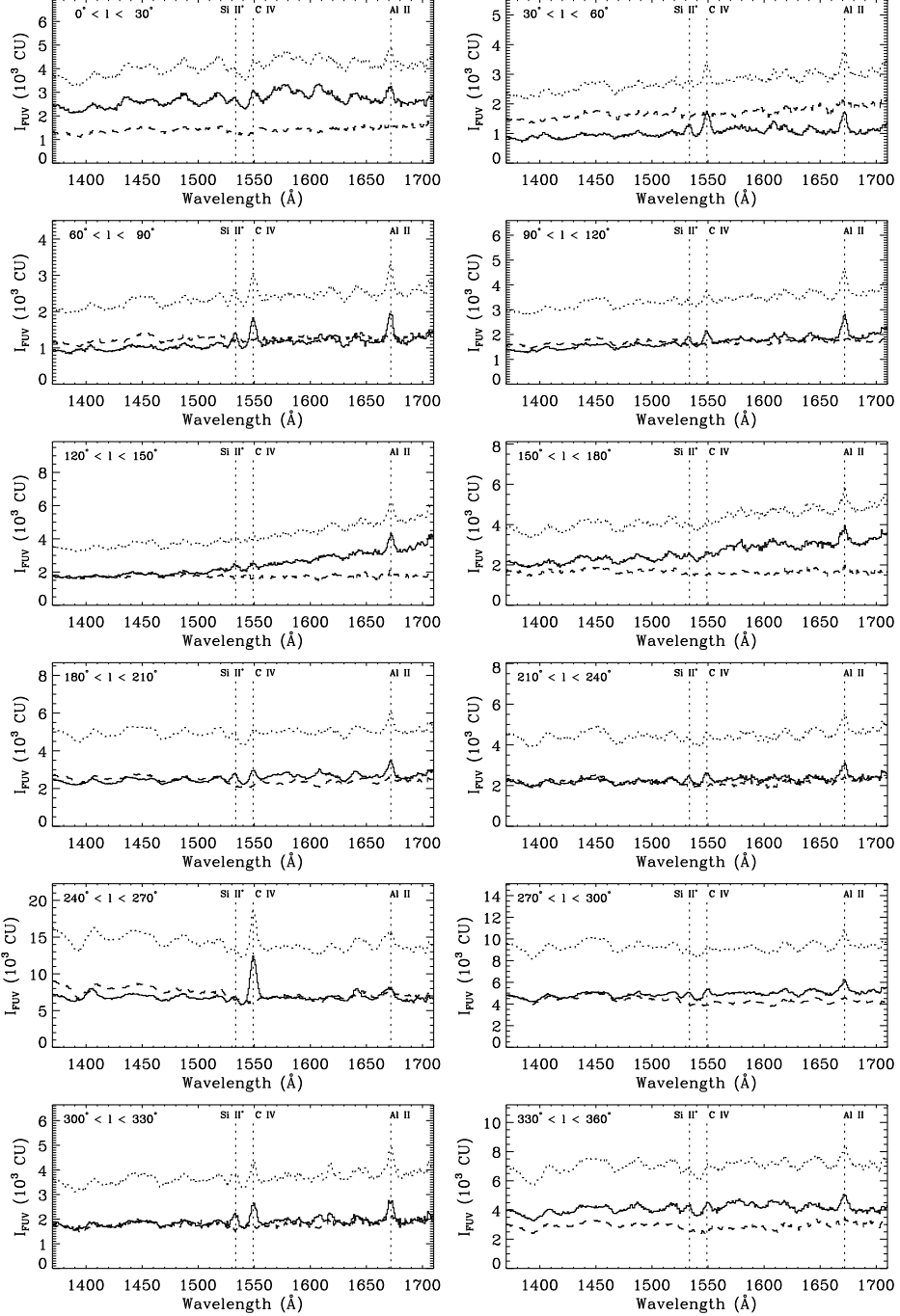


FIG. 11.— Average FUV spectra in various Galactic longitude ranges. Solid curve shows the diffuse FUV background spectrum. Dotted and dashed curves represent the total (direct stellar + diffuse) and the direct stellar spectra, respectively. Some important ionic lines are also indicated.

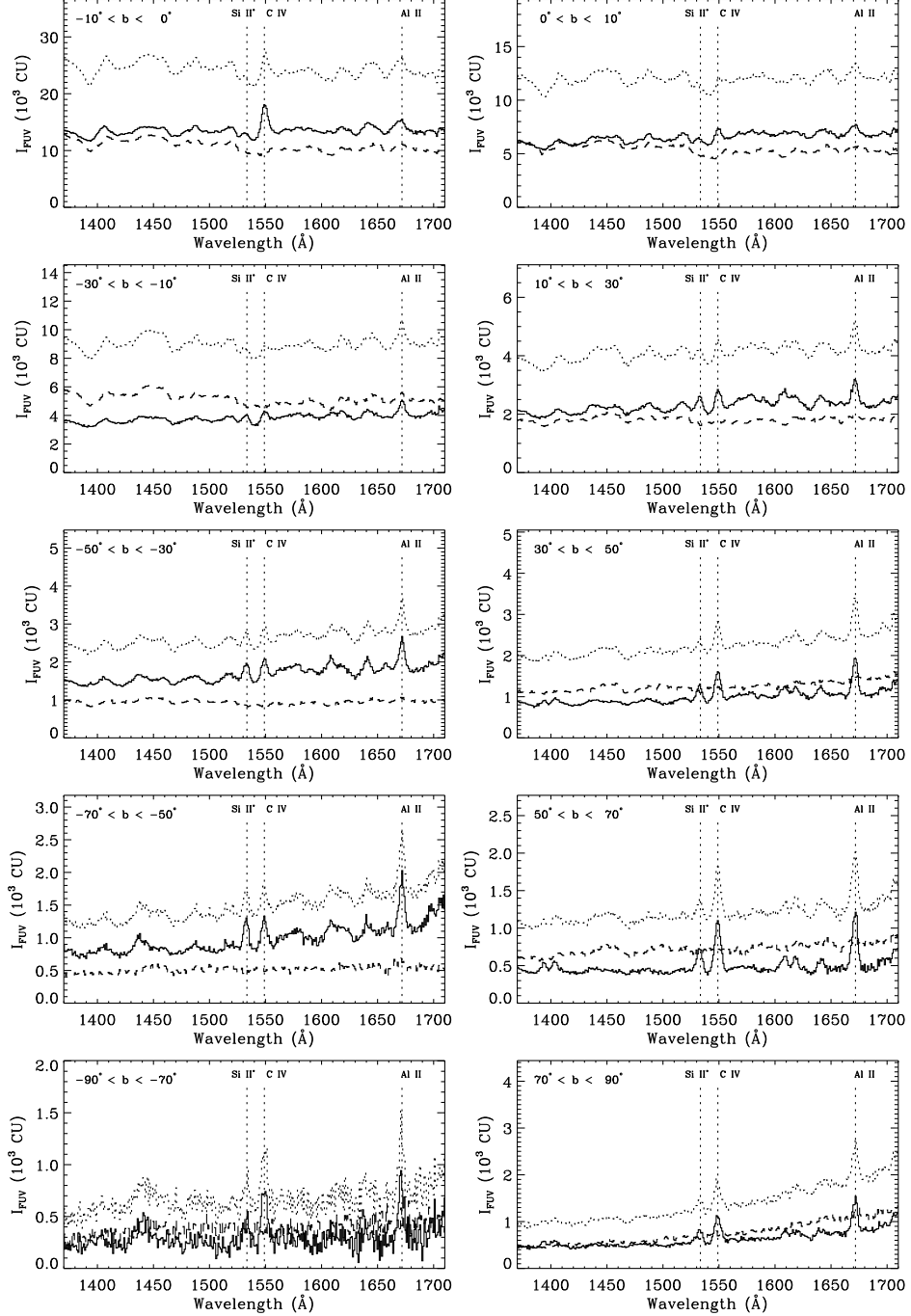


FIG. 12.— Average FUV spectra in various Galactic latitude ranges. Solid curve shows the diffuse FUV background spectrum. Dotted and dashed curves represent the total (direct stellar + diffuse) and the direct stellar spectra, respectively. Some important ionic lines are also indicated.

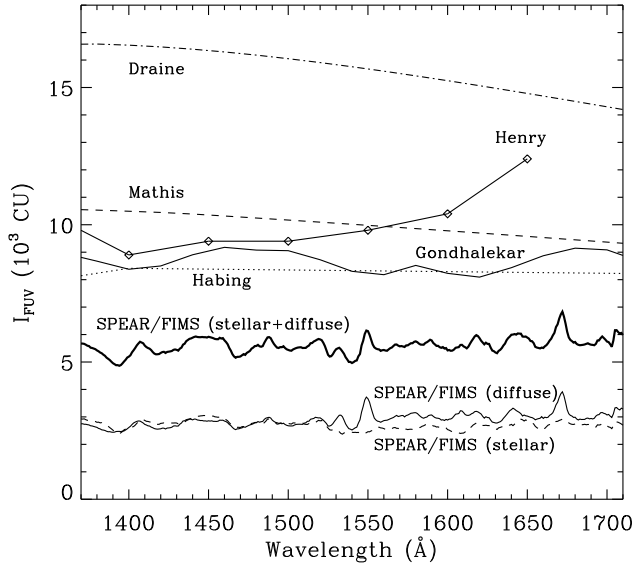


FIG. 13.— SPEAR/FIMS spectra averaged over all the observations are compared with the three models of the ISRF. The four models are from [Habing \(1968\)](#), [Gondhalekar et al. \(1980\)](#), [Draine \(1978\)](#), and [Mathis et al. \(1983\)](#). The spectrum measured by [Henry et al. \(1980\)](#) is also compared.

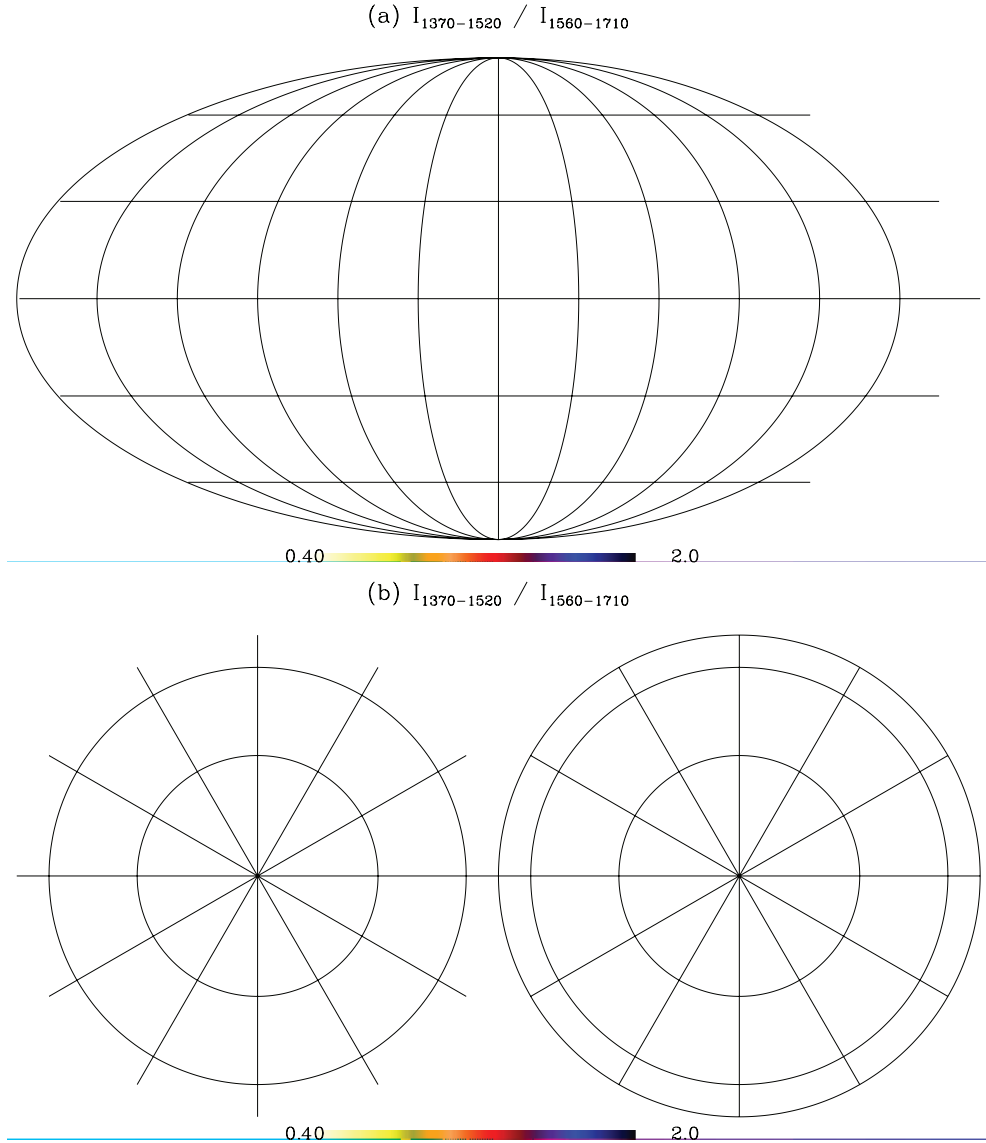
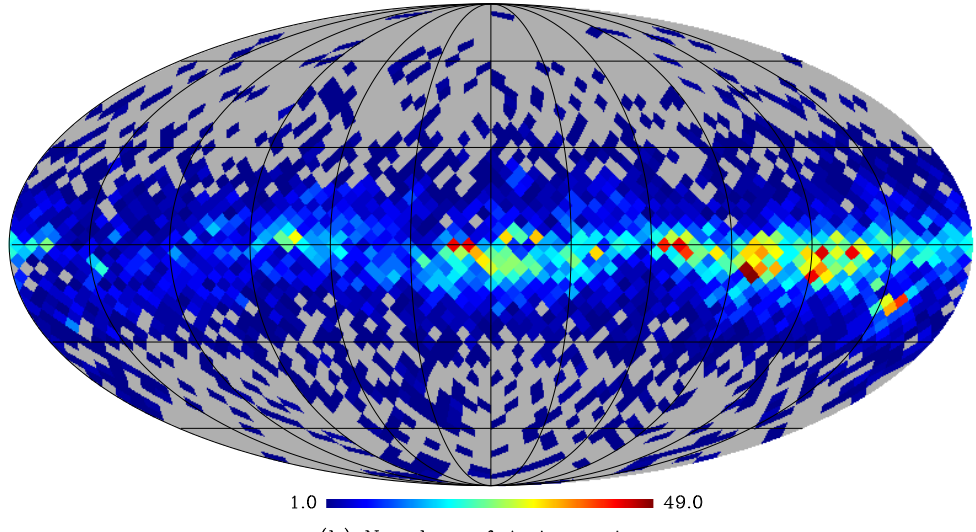


FIG. 14.— (a) Mollweide and (b) orthographic projections of the hardness ratio (1370–1520 Å to 1560–1710 Å) map. The Al II emission line was excluded in estimating the hardness ratio. The left and right sides of orthographic projections are centered at the northern and southern Galactic polar caps, respectively, and their longitude increases clockwise and counter-clockwise, respectively. In both projections, $l = 0^\circ$ is at the six o'clock position. The scales are linear across the color bars.

(a) Number of OB-type stars



(b) Number of A-type stars

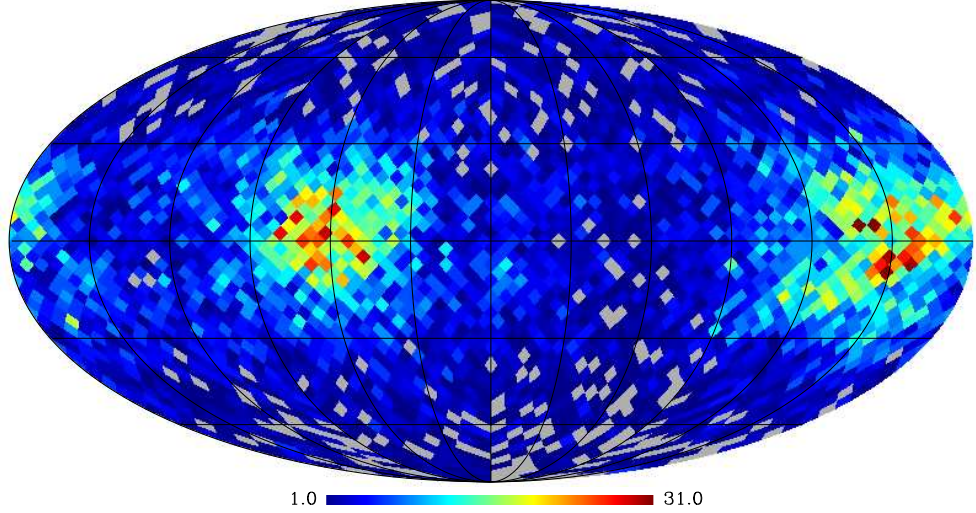


FIG. 15.— (a) Number of OB-type stars and (b) number of A-type stars from the TD-1 stellar catalog. The maps were made using the resolution parameter $N_{\text{side}} = 16$ (with $\sim 3.7^\circ$ pixels).

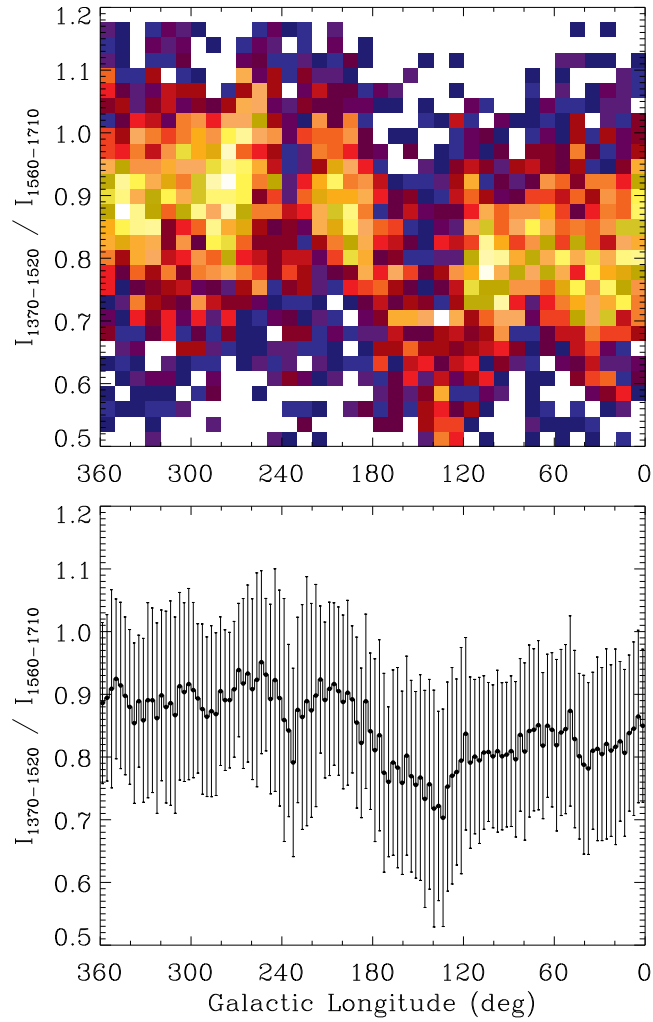


FIG. 16.— Hardness ratio (1370–1520 Å to 1560–1710 Å) versus Galactic Longitude. The Al II emission line was excluded in estimating the hardness ratio.

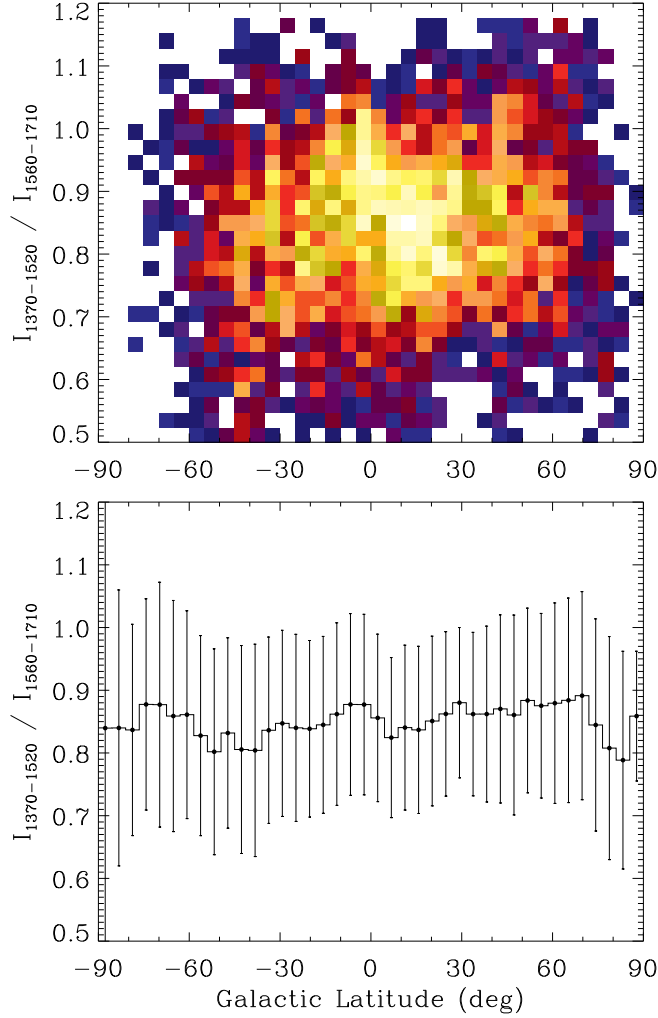


FIG. 17.— Hardness ratio (1370–1520 Å to 1560–1710 Å) versus Galactic Latitude. The Al II emission line was excluded in estimating the hardness ratio.

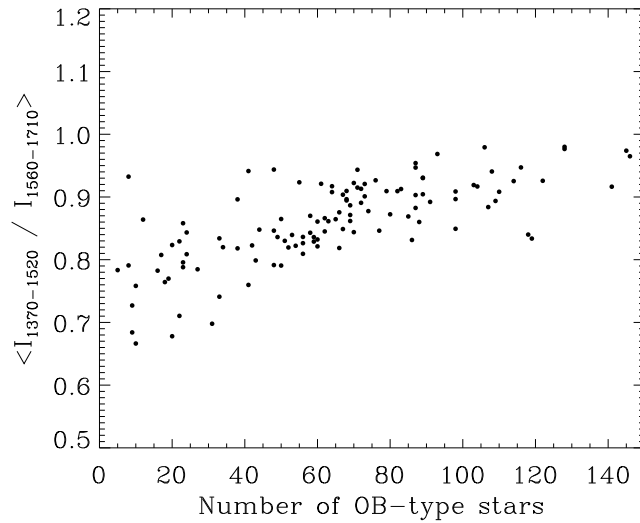


FIG. 18.— Correlation between the average hardness ratio (1370–1520 Å to 1560–1710 Å) and the number of OB-type stars. The average hardness ratio and the number of OB-type stars were calculated within each of the 3° longitude strips, and then the average hardness ratio versus the number of OB-type stars was plotted. The Al II emission line was excluded in estimating the hardness ratio.

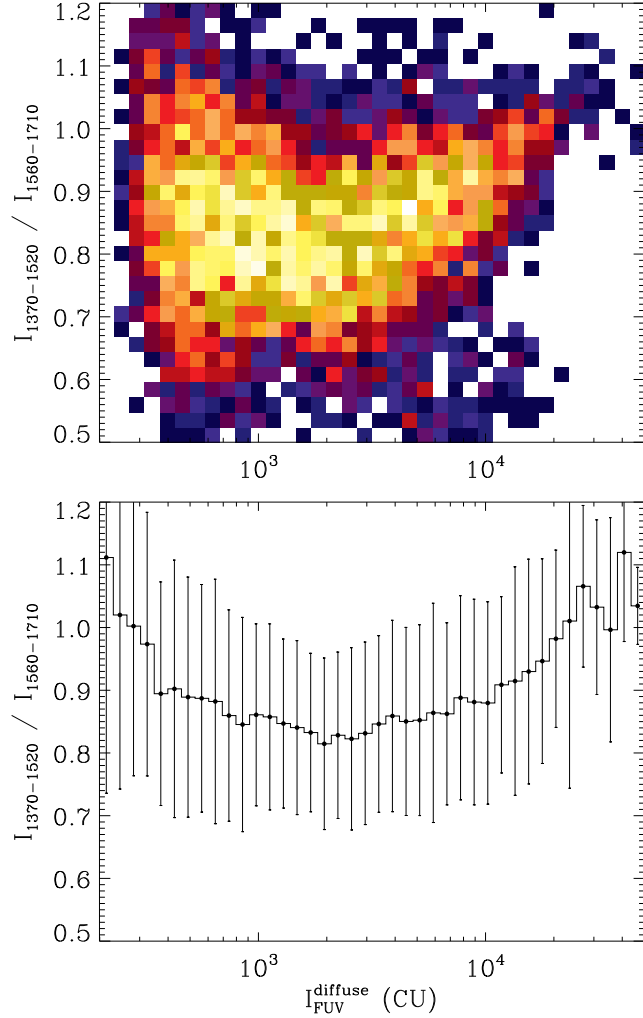


FIG. 19.— Hardness ratio (1370–1520 Å to 1560–1710 Å) versus intensity (1370–1520, 1560–1660, and 1680–1710 Å). The Al II emission line was excluded in estimating the hardness ratio.

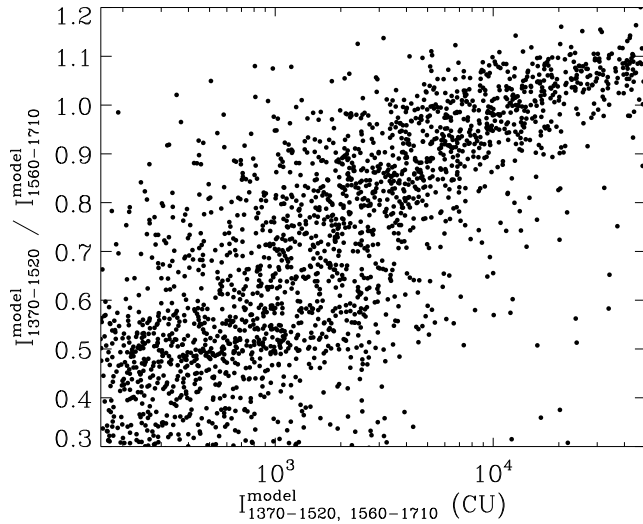


FIG. 20.— Stellar model prediction of hardness ratio (1370–1520 Å to 1560–1710 Å) versus intensity (1370–1520, 1560–1660, and 1680–1710 Å). The Al II emission line was excluded in estimating the hardness ratio.

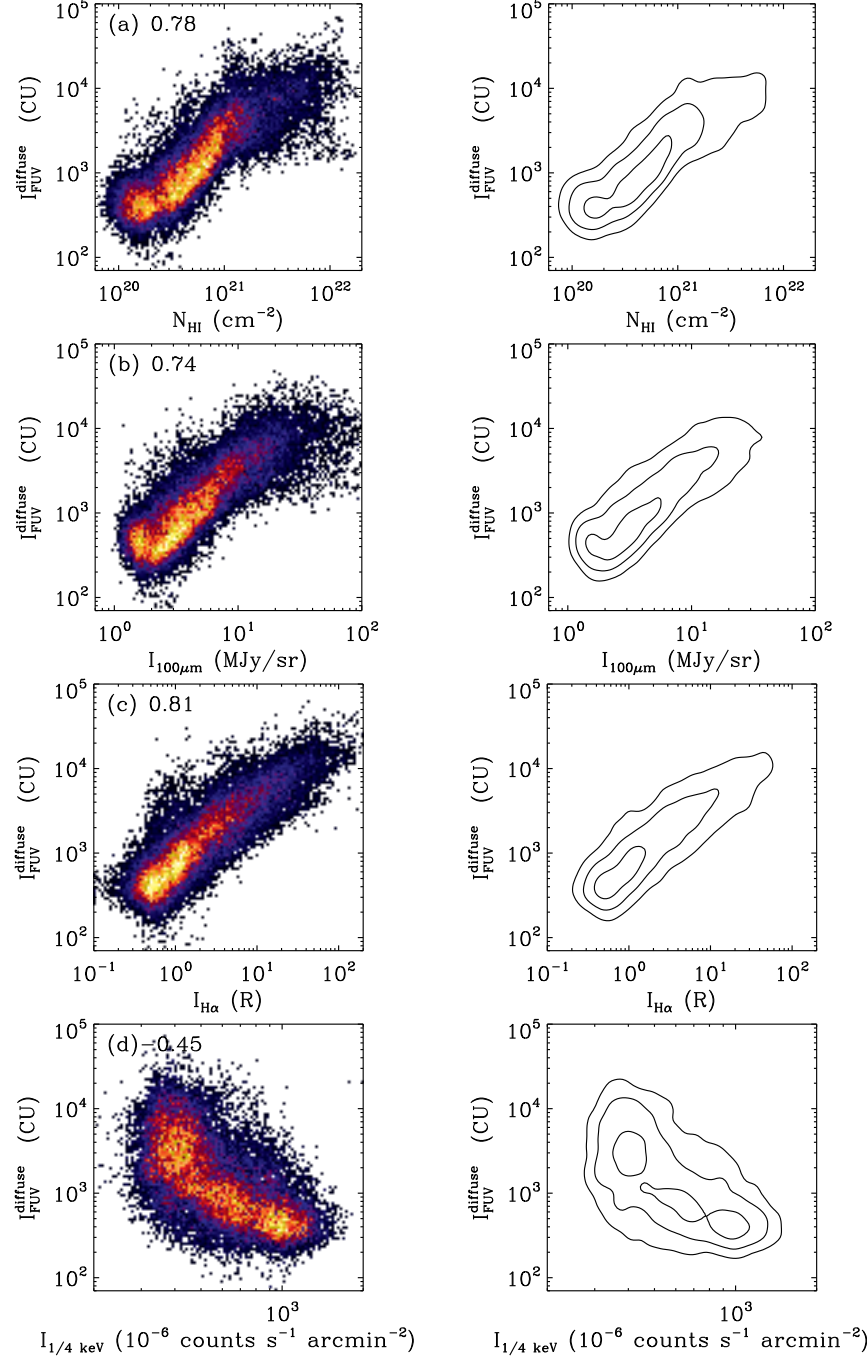


FIG. 21.— Correlation of the diffuse FUV background with (a) neutral hydrogen column density, (b) 100 μ m emission, (c) the diffuse H α emission, and (d) soft X-ray (1/4 keV band) background. The left panels show two-dimensional histogram and the right panels contours of the histograms. Numbers in the left panels are the correlation coefficients estimated in logarithmic scale. The contours correspond to 0.7, 0.3, and 0.1 of the maximum values of the histograms.

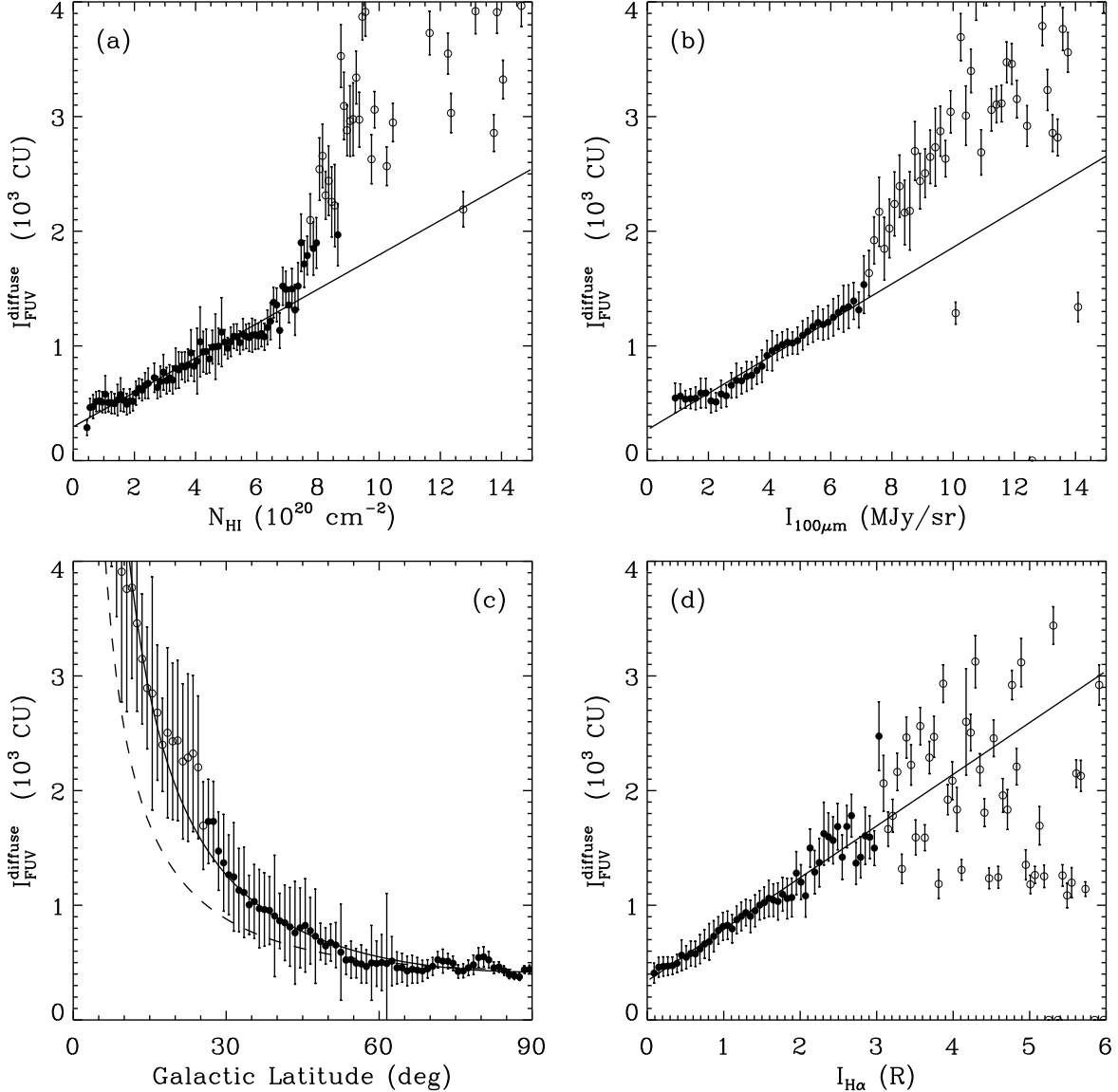


FIG. 22.— The FUV intensity versus (a) neutral hydrogen column density, (b) $100 \mu\text{m}$ emission, (c) Galactic latitude, and (d) the $\text{H}\alpha$ intensity. Best fits in (a), (b), and (d) are lines with (a) slope $1.49 \text{ CU}/(10^{18} \text{ cm}^{-2})$, offset 271 CU , (b) slope $158 \text{ CU}/(\text{MJy/sr})$, offset 243 CU , and (d) slope $456 \text{ CU}/R$, offset 309 CU . Best fit curves in (c) are $847 \text{ csc}|b| - 457 \text{ CU}$ for solid curve, and $412 \text{ csc}|b| \text{ CU}$ for dashed curve. Filled and hollow circles denote the data points, respectively, used and not used for the fit.

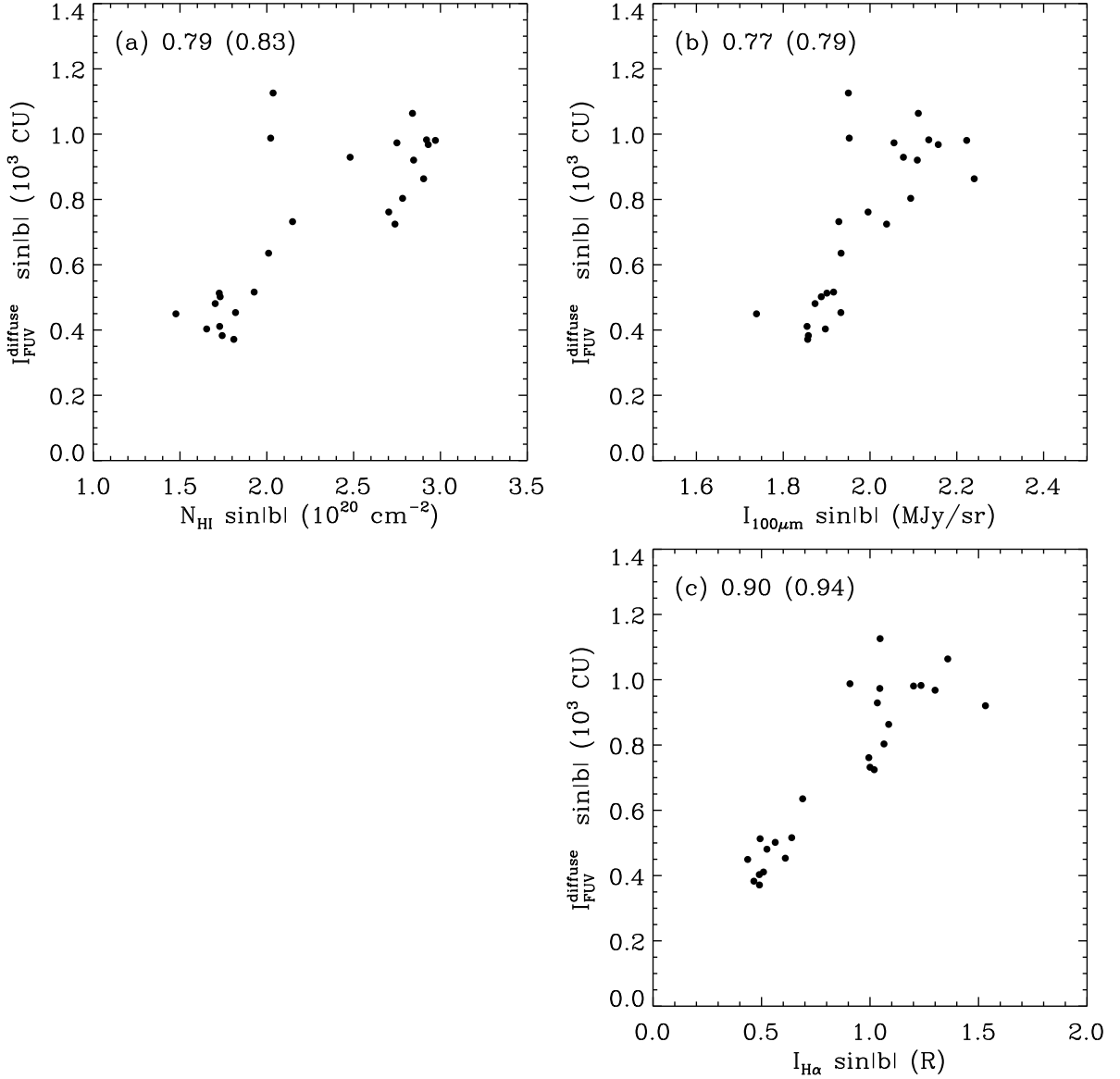


FIG. 23.— Correlation of the diffuse FUV continuum intensity with (a) neutral hydrogen column density, (b) 100 μm emission, and (c) the diffuse H α intensity after the removal of inverse- $\sin|b|$ dependence due to the plane-parallel medium. Data points were obtained from latitude ranges of $\sin|b| \geq 0.5$ ($|b| \geq 30^\circ$). Numbers outside and inside the parentheses are correlation coefficients estimated in linear and logarithmic scales, respectively.

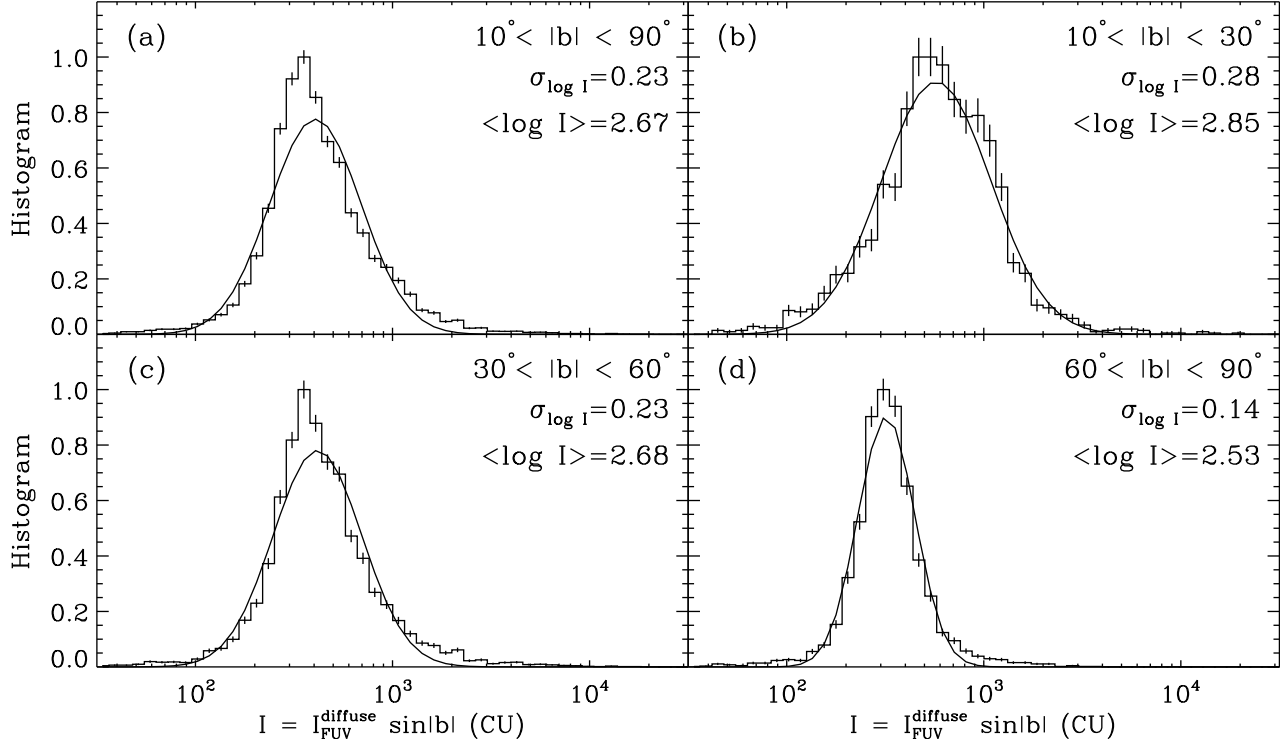


FIG. 24.— Histograms of $I_{\text{FUV}}^{\text{diffuse}} \sin|b|$ in logarithmic scale. Log-normal fits are also shown. The standard deviations and the mean values of the distribution in logarithmic scale are also shown.

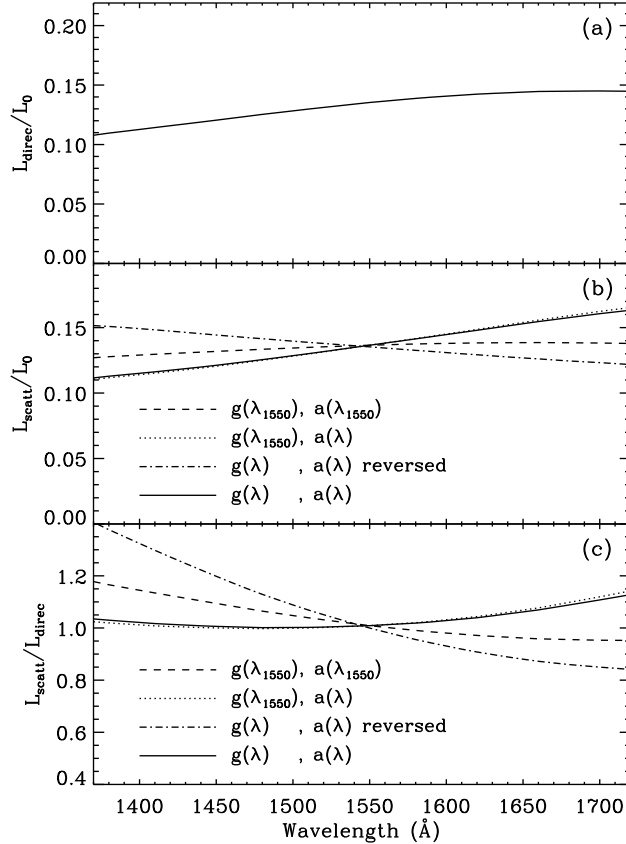


FIG. 25.— Scattering and absorption in a homogeneous dust medium. (a) The directly-escaped and (b) scattered spectra relative to the input luminosity of the point source. (c) The scattered spectrum relative to the attenuated direct stellar spectrum. Here, various combinations of the wavelength-dependences of the dust albedo and asymmetry factor are examined.

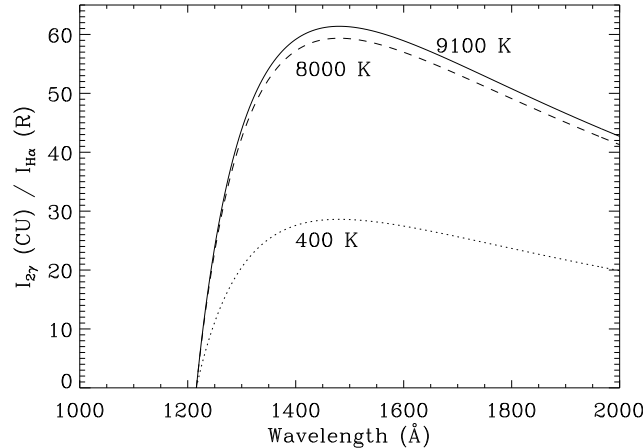


FIG. 26.— Two-photon continuum intensity that accompany 1 R of H α emission from ionized interstellar hydrogen. The continuum intensity is shown for three temperatures: 9100 K, solid line; 8000 K, dashed line; 400 K, dotted line.